Postprint of: Marzec I., Tejchman J., Mróz Z., Numerical analysis of size effect in RC beams scaled along height or length using elasto-plastic-damage model enhanced by non-local softening, Finite Elements in Analysis and Design, Vol. 157 (2019), pp. 1-20, DOI: 10.1016/j.finel.2019.01.007

Numerical analysis of size effect in RC beams scaled along height or length using elasto-plastic-damage model enhanced by non-local softening

I. Marzec[1], J. Tejchman[1] and Z. Mróz[2]

[1]Gdansk University of Technology

Gdańsk-Wrzeszcz 80-233, Narutowicza 11/12, Poland

irek@pg.edu.pl, tejchmk@pg.edu.pl

[2]IPPT, Warsaw, Poland

zmroz@ippt.pan.pl

Abstract

Numerical simulation results of laboratory tests on reinforced concrete beams subjected to four-point bending for a separate variation of the height and length were presented. Due to the lack of a geometrical similarity, two major failure mechanisms were observed: flexural failure mechanism with plastic yielding of reinforcement and shear failure mechanism with two different modes: brittle diagonal tension and brittle diagonal shear-compression. The shear strength increased with increasing effective height and decreased with increasing shear span-effective height ratio. In simulations, the finite element method was used, based on a coupled elasto-plastic-damage constitutive model for concrete under plane stress conditions. The constitutive model was enhanced by integral-type non-locality in the softening regime to yield mesh-independent results. The bond-slip law was assumed between concrete and reinforcement. Two-dimensional numerical calculations under plane stress conditions satisfactorily reproduced both experimental shear strengths and failure mechanisms with one set of input parameters. In addition, the effect of different material constants on strength and fracture was comprehensively studied. Advantages and shortcomings of the numerical approach were discussed.

Keywords: size effect; finite element method; elasto-plasticity; damage mechanics; reinforced concrete; non-local theory

1. Introduction

The size effect is a fundamental phenomenon in concrete structures. It denotes that both the: 1) nominal structural strength (corresponding to the maximal load value reached in the loading process) and 2) material ductility (ratio between the energy consumed during the loading process after and before the stress-strain peak) always decrease with increasing member size under tension [1]. These two deformation process parameters are of major importance for the assessment of the member safety and its interaction with adjacent structural members. Concrete structures exhibit a strong transition from the snap-through response in the post-critical phase for small size members to the snap-back response (a catastrophic drop in strength related to a positive slope in a stress-strain softening branch) for large size members. There exist several size effect rules for concrete [1]-[3]. The most realistic is the combined energetic-statistical size effect rule proposed by Bazant [4] that is valid for geometrically similar structures. However, the formulation of rules of limit load sensitivity of concrete and reinforced concrete members relative to both size and arbitrary shape variations is required for engineering applications. This constitutes a more difficult class of problems requiring an analysis of different failure mechanisms.

The extensive experimental studies of a size effect were performed for RC beams that were geometrically similar. A strong size effect was experimentally observed in RC beams without shear reinforcement wherein diagonal shear-tensile fracture occurred in [5]-[14]. It was predominantly of the energetic type. The experimental diagonal failure cracks had in experimental tests similar paths and relative lengths at the maximum load independently of the beam size. The size effect was also observed in reinforced concrete beams with shear reinforcement [15]-[17]. In these experiments a diagonal shear-tensile fracture [15], [16] or crushing of a compressive zone [17] took place in concrete. Thus the use of stirrups did not suppress the size effect provided the longitudinal and vertical reinforcement yielding did not occur. The effect of the varying reinforcement ratio on the failure mode in RC beams was experimentally shown by Carpintieri et al. [18]. The observed failure mode changed from longitudinal reinforcement yielding, through diagonal tension to compressive zone crushing with increasing reinforcement ratio. However, only a few papers were devoted to a size effect in RC beams with independently varying heights and lengths (e.g. [19]).

In our earlier paper [20], the novel laboratory experiments were described that were carried out on longitudinally reinforced concrete beams without shear reinforcement subjected to four-point bending.

RC beams of separately varying height and length were experimentally analyzed to investigate the size effect on a nominal strength and post-critical brittleness. Beams were scaled in the height direction in the first test series and in the length direction in the second series. Due to lack of geometrical similarity, two failure mechanisms were exhibited: flexural failure mechanism with plastic yielding of reinforcement and brittle shear mechanism in concrete with dominant normal diagonal crack displacements (so-called shear-tension failure mode) or with simultaneous significant normal and tangential diagonal crack displacements (so-called shear-compression failure mode). Load-deflection diagrams and crack paths were registered during experiments. The digital image correlation (DIC) technique was applied to visualize strain localization on the concrete surface. In addition, the crack opening and crack slip displacements on the beam surface were measured. The experimental results showed pronounced differences as compared with strut-and-tie models following ACI [21] and Zhang and Tan [22]. The alternative formulae based on the modification of these models slightly improved the agreement [20].

The goal of the present paper is to offer numerical simulations of the beam response by the finite element (FE) model and to relate them to our laboratory tests on reinforced concrete beams subjected to four-point bending (with respect to strength and fracture) by taking different failure mechanisms into account. Usually, the size effect has been investigated in concrete and concrete structural elements that are geometrically similar and exhibit the same failure mechanism. The attention was paid to the reproduction of the: 1) size effect related to the beam strength, 2) fracture process and 3) failure modes of diagonal tension and diagonal shear compression.

Two-dimensional (2D) finite element (FE) analyses under plane stress conditions were performed with the coupled elasto-plastic-damage constitutive model for concrete. The damage (e.g. [23]-[25]) and coupled elasto-plastic damage formulations (e.g. [26-33]) were widely used to describe the concrete fracture behaviour under various loading conditions. The formulations presented a simplified isotropic (e.g. [23]-[26]) or a more realistic anisotropic damage concept (e.g. [26], [27], [29], [30], [33]).

The formulation in the current paper was enhanced by a characteristic length of micro-structure with the aid of integral-type non-locality in the softening regime. The non-local theory allows for reproducing fracture patterns independently of the mesh for both localized and distributed cracking, and the numerical results are insensitive to the finite element mesh size and alignment. The bond-slip rule between concrete and reinforcement was assumed in FE analyses. The effect of different material constants on strength

and fracture was comprehensively studied. Our focus was on a relationship between tangential and normal displacements along a critical diagonal crack in RC beams which failed in shear.

Recently, the analogous constitutive model has been successfully used in investigations of the size effect and related fracture in geometrically similar concrete beams with basalt reinforcement [34]. This model was also applied to RC concrete beams under mixed shear-tension failure [35] and composite RC-EPS slabs under shear failure [36]. In the current paper, the constitutive model for concrete was slightly improved.

2. Overview of experimental program

2.1 General information

The laboratory tests of four-point bending were conducted on rectangular concrete beams with longitudinal steel ribbed bars without shear (vertical) reinforcement [20].

The beams were scaled along either the height D (series '1', Tab.1, Fig.1A,) or length l_{eff} (series '2', Tab.1, Fig.1B). The thickness of all beams was t=0.25 m to avoid differences in the hydration heat effects that are proportional to the member thickness. The beam deformation and failure were characterized by two non-dimensional geometric parameters and one size parameter: $\eta_a=a/D$, $\eta_b=b/D$, $\eta_l=l_{eff}/D=2\eta_a+\eta_b$. The reinforcement ratio $\eta_r=A_r/A_b$ was constant for the varying cross-sectional area A_b of the beam. The concrete cover (c=4 mm) was large enough to prevent the bond failure of a splitting type. Thus, the distance from the bar centre to beam bottom was always $c'=h-D$=50 mm. For two reinforcement layers, this distance was c'=75 mm. The reinforcement location parameter $\eta_c=c'/D$ varied between 0.10-0.28 (series'1') or was fixed at 0.14 (series '2').

The beams of the series '1' were scaled along the effective height D in the proportion 1:2:4 with the constant effective span length l_{eff}=2700 mm (Fig.1A, Tab.1). The beams were denoted as S1D18a108, S1D36a108 and S1D72a108, where the symbol S1 denotes the series '1', D - the effective beam depth in [cm] and a - the shear zone length in [cm]. The beam S1D36a108 (D=360 mm) was twice as high as the beam S1D18a108 (D=180 mm) and twice as small as the beam S1D72a108 (D=720 mm). Thus, the shear zone length a and bending zone length b (distance between two concentrated forces F) were constant a=1080 mm and b=540 mm, respectively (Fig.1A). The shear span parameter $\eta_a=a/D$ was 1.5,

3 and 6, the length parameter $\eta_l=l_{eff}/D$ was 3.75, 7.5 and 15 and the bending span parameter $\eta_b=b/D$ was 0.75, 1.5 and 3. Each beam height h included 3 identical concrete specimens to verify the result repeatability (indicated as: S1D18A108_1 - S1D18a108_3, S1D36a108_1 - S1D36a108_3 and S1D72a108_1 - S1D72a108_3).

The beams of the series '2' had the same height (D=360 mm) but varying effective span length l_{eff} and shear span a (the latter scaled in the proportion 1:2:3) (Fig.1B, Tab.1). The beams were denoted as S2D36a36 (a=360 mm), S2D36a72 (a=720 mm) and S2D36A108 (a=1080 mm) with the length parameter $\eta_l=l_{eff}/D$=3.5, 5.5 and 7.5, the shear span parameter $\eta_a=a/D$=1.0, 2.0 and 3.0 and the bending span parameter $\eta_b=b/D$=1.5. The longest beam from the series '2' (S2D36a108) had the same dimensions as the beam from the series '1' denoted as S1D36a108. The beam S2D36a36 was as twice as short as the beam S2D36a72 and the beam S2D36a108 was as twice as long as the beam S2D36a72. Each beam included 2 identical members (denoted as: S2D36a36_1 - S2D36a36_2, S2D36a72_1 - S2D36A72_2, S2D36a108_1 - S2D36a36_2).

In total 15 beams (series '1': 9 beams and series '2': 6 beams) were subjected to four-point bending. The ratio of the shear span a to the effective height D varied from $\eta_a=a/D$=1 up to η_a=6, thus different failure modes were expected to be developed. The ratio of the bending span b to the effective height D varied from $\eta_b=b/D$=0.75 up to η_b=3 (series '1') and η_b=1.5 (series '2').

The reinforcement of all beams consisted of ribbed bars of the diameter ϕ=20 mm with the mean yielding stress of σ_y=560 MPa (class B500) and the modulus of elasticity of 205 GPa. The longitudinal reinforcement ratio was designed as ρ_L=1.4% ($\rho_L=A_{SL}/(bD)$, A_{SL} – the cross-section area of longitudinal reinforcement). Each beam size required a different number of bars depending on the effective depth D. The beams of D=18 cm and D=36 cm had 2 and 4 bars in one layer, respectively. The beam of D=72 cm had two layers with 4 bars i.e. 8 bars in total (Fig.1C). In order to avoid the anchorage zone failure, hooked steel bars were used (Fig.1) with the anchorage length of 130 mm, 310 mm or 670 mm, depending on the beam height.

Three accompanying tests were performed, including uniaxial compression of the concrete cubes (150×150×150 mm^3) and splitting tension and elastic compression of the concrete cylinders (ϕ=150 mm and L=150 mm). The measured average characteristic compressive strength on cubes was f_c=61.5 MPa.

Thus, the corresponding concrete class was C45/55. The average characteristic splitting tensile strength was f_t=3.21 MPa. The measured average elastic modulus was E=34.2 GPa. The tests were performed under displacement-controlled conditions. The steel loading plates were always used in order to avoid local concrete crushing. Their area was always the same, i.e. 100×250 mm^2 (l_a×t). The area of support (bearing) plates (l_b×t) had also the same size. During the test, the vertical force and displacements were measured. The true deflection at the mid-span and support displacement were registered by means of linear variable displacement transducers (LVDT's). The steel strains were traced with strain gauges placed on reinforcement bars at the beam mid-span. The front side of the beam was prepared to track cracks and to measure their width with a simple microscope. A detailed description including the crack opening ω and slip displacements δ were calculated based on measurements with a digital extensometer of DEMEC type with the base of 100 mm. The measuring mesh consisting of equilateral triangles which covered the area where a critical diagonal crack was expected to appear. The number of triangles varied between particular series depending on the beam size. During tests, the elongation of triangle sides (AB, AC and BC) was measured and the crack trajectory was registered.

2.2 Experimental results on strength and fracture

The shear strength of beams evidently decreased with increasing both parameters η_a=a/D and η_l=l_{eff}/D. It also decreased with increasing parameter η_b from 0.75 to 1.5 in beams with varying effective depth and constant effective length. The shear strength's increase was extremely large (250%) in the range of η_a=1.0 (η_l=3.5) and η_a=1.5 (η_l=3.75).

Two different failure mechanisms were observed in the RC beams (Fig.2): plastic flexural failure mechanism characterized by reinforcement yielding for η_a=6 (η_l=15, η_b=3) (Fig.2a) and shear failure mechanism in concrete for η_a=1-3 (η_l=3.5-7.5, η_b=0.75-1.5) (Figs.2b-f). For the lower value of η_a=2-3 (η_l=5.5-7.5, η_b=1.5), the so-called diagonal tension failure mode dominated (Figs.2b and 2d), i.e. the normal displacements were always larger than the tangential displacements along the critical diagonal crack. In the case of the lowest values of η_a=1-2 (η_l=3.5-5.5, η_b=0.75-1.5), so-called shear-compression failure mode dominated (Figs.2c, 2e and 2f), i.e. the normal displacements were always smaller than the tangential displacements in the top beam region of the critical diagonal crack. The distance between the critical diagonal crack and beam support d_c related to the shear span a varied between d_c/a=0.5 for low beams (η_a=3) up to as d_c/a=0 for high beams (η_a=1). For the RC beam S2D36a36, concrete spalling in

the compressive zone above the critical diagonal crack was also observed.

For high beams, the strut-and-tie models following ACI [20] and Zhang and Tan [21] overestimated the shear strength for η_a=1.5-2 (by 20%-100%) and underestimated for η_a=1 (by 5%-25%). The difference between the experimental and theoretical results by ACI and Zhang and Tan increased with decreasing η_a. The alternative formulae [19] based on the modification of the strut-and-tie model significantly improved the theoretical results in the range of η_a=1.5-2, but at the same time strongly worsened the results for η_a=1.

The discrepancies between the experimental and theoretical results (based on the strut-and-tie models) according to [19] were caused by: a) the varying strut widths and strut inclinations for all high beams with η_a=1-2 and b) the different shapes of compressive struts for the beams with η_a=2. The clear disadvantage of strut-tie models was that they were not able to distinguish between 2 different failure modes in shear (diagonal tension and shear compression) which affected the beam strength to a different grade.

3. Numerical approach

3.1 Concrete description

The coupled isotropic elasto-plastic-damage constitutive model was proposed for monotonic and cyclic loading of concrete [35]-[39]. Plasticity and scalar damage were combined assuming the so-called strain equivalence hypothesis [40]. The elasto-plasticity was defined in terms of the effective stress according to

$$\sigma_{ij}^{eff} = C_{ijkl}^{e}\varepsilon_{kl} \,. \tag{1}$$

where σ_{ij}^{eff} is the effective stress tensor, C_{ijkl}^{e} denotes the elasticity tensor for the undamaged material and ε_{kl} is the strain tensor. In an elasto-plastic regime, the failure surface was assumed as a combination of two surfaces [41], [42]. In compression, the shear yield surface based on the linear Drucker-Prager criterion with isotropic hardening and softening was used [43]

$$f_1 = q + p\tan\varphi - \left(1 - \frac{1}{3}\tan\varphi\right)\sigma_c(\kappa_1)\,, \tag{2}$$

where q is the Mises equivalent deviatoric stress, p denotes the mean stress and φ is the internal friction angle. The evolution of material hardening/softening related to growing effective strain κ_1 was defined by the uniaxial compression yield stress $\sigma_c(\kappa_1)$. The internal friction angle φ was assumed as [43]

$$\tan\varphi = \frac{3(1 - r_{bc}^{\sigma})}{1 - 2r_{bc}^{\sigma}}\,, \tag{3}$$

where r_{bc}^{σ} is the ratio between the biaxial compressive strength and uniaxial compressive strength ($r_{bc}^{\sigma} = 1.2$). The invariants q and p are

$$q = \sqrt{\frac{3}{2}s_{ij}s_{ij}} \quad \text{and} \quad p = \frac{1}{3}\sigma_{kk}\,, \tag{4}$$

where σ_{ij} is the stress tensor and s_{ij} denotes the deviatoric stress tensor. The flow potential was defined as

$$g_1 = q + p\ \tan\psi\,, \tag{5}$$

where ψ is the dilatancy angle ($\psi \neq \varphi$). For the sake of simplicity, the constant values of φ and ψ were assumed. In tension, the Rankine criterion was used with a yield function f_2 [41], [42] with isotropic softening defined as

$$f_2 = \max\{\sigma_1, \sigma_2, \sigma_3\} - \sigma_t(\kappa_2)\,, \tag{6}$$

where σ_i– the principal stress, $\sigma_t(\kappa_2)$ – the tensile yield stress and κ_2 – the hardening/softening parameter equal to the maximum principal plastic strain ε_1^p. The associated flow rule was assumed. The edges and vertices in Rankine yield function were taken into account by the interpolation of 2-3 plastic multipliers according to the Koiter's rule. The same procedure was adopted in the case of combined tension (Rankine criterion) and compression (Drucker-Prager criterion). For both yield stress functions $\sigma_c(\kappa_1)$ and $\sigma_t(\kappa_2)$,

the linear hardening was assumed with the plastic hardening modulus $H_p = E/2$. The graphic interpretation of failure surface for the coupled Drucker-Prager-Rankine criterion is presented in Fig.3.

The material degradation was calculated within isotropic damage mechanics, independently in tension and compression using one equivalent strain measure$\tilde{\varepsilon}$ by Mazars [24] (ε_i - principal strains)

$$\tilde{\varepsilon} = \sqrt{\sum_{\mathrm{i}} \langle \varepsilon_{\mathrm{i}} \rangle^2} \quad . \tag{7}$$

The equivalent strain measure $\tilde{\varepsilon}$ may be defined in terms of elastic or total strains [41]. The stress-strain relationship was represented by the following formula

$$\sigma_{ij} = (1 - D)\sigma_{ij}^{eff}, \tag{8}$$

with the term '1-D' defined as:

$$(1 - D) = (1 - s_c D_t)(1 - s_t D_c) \ , \tag{9}$$

where

$$D_t = 1 - \frac{\kappa_0}{\kappa_t}\left(1 - \alpha + \alpha e^{-\beta(\kappa_t - \kappa_0)}\right) \ , \tag{10}$$

$$D_c = 1 - \left(1 - \frac{\kappa_0}{\kappa_c}\right)\left(0.01\frac{\kappa_0}{\kappa_c}\right)^{\eta_1} - \left(\frac{\kappa_0}{\kappa_c}\right)^{\eta_2} e^{-\delta_c(\kappa_c - \kappa_0)} \ , \tag{11}$$

$$s_t = 1 - a_t \omega\left(\sigma_{ij}^{eff}\right) \quad \text{and} \quad s_c = 1 - a_c\left(1 - \omega\left(\sigma_{ij}^{eff}\right)\right) \ , \tag{12}$$

$$\kappa_t = \kappa\omega\left(\sigma_{ij}^{eff}\right) \quad \text{and} \quad \kappa_c = \kappa\left(1 - \omega\left(\sigma_{ij}^{eff}\right)\right) \ , \tag{13}$$

$$\omega\left(\sigma_{ij}^{eff}\right) = \begin{cases} 0 & \text{if} \quad \sigma_i^{eff} = 0 \\ \dfrac{\sum\langle\sigma_i^{eff}\rangle}{\sum\left|\sigma_i^{eff}\right|} & \text{otherwise} \end{cases} \quad . \tag{14}$$

The damage functions D_t and D_c describe the damage evolution under tension [44] and compression [45] by means of the following material constants: α, β, η_1, η_2 and δ_c. The threshold parameter κ was defined as the maximum of the equivalent strain measure $\tilde{\varepsilon}$ reached during the load history up to time t: $\kappa(t) = \max_{\tau<t} \tilde{\varepsilon}(\tau)$. In contrast to our previous constitutive concrete model [35]-[39], the damage under tension

was here separately controlled in FE simulations by the threshold parameter κ_t and the damage under compression separately by the threshold parameter κ_c. The damage function under tension D_t solely evolved for the threshold parameter $\kappa_t \geq \kappa_0$ and the damage function under compression D_c evolved only for the threshold parameter $\kappa_c \geq \kappa_0$. For the threshold parameters $\kappa_t \leq \kappa_0$, $\kappa_c \leq \kappa_0$, there was no damage growth under tension and compression ($D_t = D_c = 0$). The splitting factors are a_t and a_c, and $\omega\left(\sigma_{ij}^{eff}\right)$ denotes the stress weight function [46]. Thus, under pure tension the stress weight function was $\omega\left(\sigma_{ij}^{eff}\right) = 1$ and the growth of damage under pure tension was solely influenced by the evolution of D_t. The Mac Cauley bracket in Eq.14 is defined as $\langle x \rangle = (x + |x|)/2$. The constitutive model with a different stiffness in tension and compression and a positive-negative stress projection operator to simulate crack closing and crack re-opening is thermodynamically consistent. It shares main properties of the model by Lee and Fenves [46], which was proved to be consistent with thermodynamic principles (plasticity is defined in the effective stress space, isotropic damage is used and the stress weight function is continuous). Carol and Willam [47] showed that for damage models with crack-closing-re-opening effects, only isotropic formulations did not suffer from spurious energy dissipation under non-proportional loading in contrast to anisotropic ones.

Due to the small thickness of beam , the plane stress condition (out of plane stress components equal to zero) was a natural choice for numerical modelling. In plasticity the plane stress-projected method was used and the plane stress elasticity matrix was applied in the analysis. For calculations of the equivalent strain measure, the out-of-plane normal strain was determined. In tension, the result differences between plane strain and plane stress were negligible. In compression, the strength for plane strain state was higher by about 20% than for plane stress state due to the presence of the out of plane stress.

In the case of linear hardening model, the following 16 material constants are required: E, υ, κ_0, α, β, η_1, η_2, δ_c, a_t, a_c, ψ, φ, initial yield stresses σ_{yt}^0 (tension) and σ_{yc}^0 (compression) and plastic hardening moduli H_p (in compression and tension). The quantities σ_{yt}^0 (initial yield stress during hardening) and κ_0 are responsible for the peak location on the stress-strain curve and a simultaneous activation of the plasticity and damage criteria. The shape of the stress-strain curve in softening is influenced by the constant β in tension, and by the constants δ_c and η_2 in compression. The stress-strain curve at the residual state is affected by the constant α in tension and by the constant η_1 in compression. Since the compressive stiffness is recovered upon the crack closure as the load changes from tension to compression, and the

tensile stiffness is not recovered due to compressive micro-cracks, the damage splitting factors a_c and a_t may be taken for the sake of simplicity as a_t=0 and a_c=1.0. The equivalent strain measure $\tilde{\varepsilon}$ (Eq.7) was defined in terms of total strain following [40]. A simple cyclic tension-compression-tension element test was performed to show the model response under the load reversal (Fig.4). The 1D concept of the stiffness recovery with the limit damage splitting factors a_t and a_c (value 0 or 1) was shown in Fig.4a. Figure 4b presents the stress-strain curves for two full load cycles with three different sets of the damage splitting factors (a_t=0 and a_c=1.0, a_t=0 and a_c=0.8 and a_t=0.2 and a_c=1.0). The load began in tension, next it changed to compression (below the compressive strength), then back to tension and finally to compression (above the compressive strength) and tension. The stress-strain diagrams for two different loading scenarios are shown in Fig.4c with the damage splitting factors a_t=0.2 and a_c=0.8. For the first loading scenario (blue curves), the load started in tension (curve '1'), then it moved to compression above the strength limit (curve '2') and next back to tension (curve '3'). For the second loading scenario (red curves), the load started in compression below the compressive strength (curve '1'), next moved to tension above the tensile strength (curve '2'), and then back to compression above the compressive strength (curve '3') and to tension (curve '4').

The results of Fig.4 show the different stiffness degradation in compression and tension (the degradation was stronger in tension). The effect of the damage splitting factors a_t and a_c on the stress-strain diagram under tension-compression-tension-compression was more noticeable in compression (Fig.4b). The compressive stiffness was recovered upon the crack closure as the load moved from tension to compression, and the tensile stiffness was not recovered as the load moved from compression to tension due to crushing micro-cracks with a_c=1 and a_t=0 (Fig.4b). For a_c=0.8 and a_t=0 (Fig.4b), a decrease of the factor a_c from 1.0 to 0.8 lead to a not-full recovery of the compressive stiffness in a transition from tension to compression. An increase of the factor a_t from 0.0 to 0.2 (a_t=0.2 and a_c=1.0, Fig.4b) contributed to the slightly larger tensile stiffness during a transition from compression to tension. The influence of stiffness degradation due to compressive cracks is seen in Fig.4c (a_t=0.2 and a_c=0.8). When the load moved from compression to tension (red curve '2'), the tensile stiffness was not fully recovered due to damage in compression. The compressive stiffness was not also fully recovered during a transition from tension to compression (blue curve '2'). The constitutive model was carefully validated in element tests [37], e.g. for uniaxial cyclic compression and four-point cyclic bending under tensile failure (Fig.5). The results of numerical calculations during cyclic element tests were in satisfactory agreement with the experimental outcomes [48], [49] (Fig.5).

Figure 6 shows the stress-strain diagrams under cyclic uniaxial tension and cyclic uniaxial compression for the different important material constants η_2, δ_c, β, and κ_0 (which were independently changed). The stress-strain results indicate that the parameter κ_0 is responsible for a peak location and a simultaneous activation of plastic and damage criteria. The parameter β affects model response in softening during tension and parameters δ_c and η_2 affect model response in softening during compression. In addition the parameter η_2 affects the hardening curve in compression. The effect of two other parameters (α and η_1) describing the stress-strain curve at the residual state is negligible.

The material constants E, ν, κ_0, β, α, η_1, η_2, δ_c and two hardening yield stress functions should be determined for concrete by means of two independent simple monotonic tests: uniaxial compression test and uniaxial tension (or three-point bending) test for the already fixed damage splitting factors a_t and a_c. The precise determination of the damage scale factors a_t and a_c requires one full cyclic compressive test and one full cyclic tensile (or three-point bending) test. In addition, the values of φ and ψ can be determined from triaxial compression tests [40]. The material constants were fitted to the experimental uniaxial compressive strength of concrete f_c=61.5 MPa, experimental tensile strength of concrete cylinders during splitting tension f_t=3.2 MPa and experimental modulus of elasticity of E=34 GPa. Due to the lack of laboratory full stress-strain curves during uniaxial compression and uniaxial tension, the tensile G_f and the compressive fracture energy G_c were assumed based on the literature data. The following set of the material parameters was thus assumed for monotonic FE calculations: E=34 GPa and ν=0.2, $\sigma_{yt}^0 = 3.3$ MPa, $\sigma_{yc}^0 = 60$ MPa, H_p=17 GPa, κ_0=9×10^{-5}, ϕ=14° [40], ψ=8°, β=85, α=0.95, η_1=1.15, η_2=0.15 and δ_c=150 with a_t=0 and a_c=1. Using the assumed material constants, the tensile fracture energy was G_f=100 N/m (typical value for concrete) and compressive fracture energy G_c=4000 N/m (G_c/G_f=40). The concrete behaviour during simple cyclic element tests in uniaxial compression, tension and simple shear with the assumed material parameters is shown in Fig.7. The calculated maximal uniaxial compressive strength was f_c=60 MPa (Fig.7a), maximal uniaxial tensile strength was f_t=3.2 MPa (Fig.7b) and maximal shear strength was τ_{max}=11 MPa ($\tau_{max} \approx \sqrt{f_c f_t}$) (Fig.7c).

3.1 Non-local approach

Standard constitutive laws are not able to describe properly strain softening of the material when using FEM that results in pathological sensitivity of the numerical solution to the size and alignment of finite elements. Since these laws contain no information about the size and spacing of localization zones, their

enrichment by a characteristic length of micro-structure (related to the size and spacing of material heterogeneities) is necessary. The characteristic length restores also the well-posedness of boundary value problems and makes the FE results mesh-independent. An integral-type non-local theory in the integral format was used as a regularization technique in order to describe properly strain localization and to capture a deterministic size effect (dependence of the nominal strength on the structure size) [50]-[53]. In this approach, the principle of local action does not hold. The introduction of non-locality does not violate thermodynamic principles [54]. In the calculations the equivalent strain measure the $\tilde{\varepsilon}$ in damage region was replaced by its non-local definition $\bar{\varepsilon}$ [55]

$$\bar{\varepsilon} = \frac{\int_V w(\|\boldsymbol{x}-\boldsymbol{\xi}\|)\tilde{\varepsilon}(\boldsymbol{\xi})\mathrm{d}\boldsymbol{\xi}}{\int_V w(\|\boldsymbol{x}-\boldsymbol{\xi}\|)\mathrm{d}\boldsymbol{\xi}} \,. \tag{15}$$

The Gauss distribution function was used as a weighting function w [50]

$$w(r) = \frac{1}{l_c\sqrt{\pi}} e^{-\left(\frac{r}{l_c}\right)^2} \,, \tag{16}$$

where l_c is a characteristic length of micro-structure and the parameter r denotes the distance between material points. The averaging in Eq.16 was restricted to a small representative area around each material point (the influence of points at the distance of r=3×l_c was only of 0.01%). The function in Eq.15 satisfies the normalizing condition [50]. In order to accelerate the calculations, the non-local averaging was performed solely in the neighbourhood of integration points (limited to the distance of 3l_c). Different techniques (e.g. symmetric local correction approach, distance-based and stress-based model) may be used to calculate softening non-local parameters near boundaries in order to remove an excessive energy dissipation (particularly pronounced for notched specimens) [55], [56]. The distance-based model seems to be the most realistic since it provides a good agreement for both unnotched and notched beams with the same set of parameters [56]. When calculating non-local quantities close to notches the so-called "shading effect" is considered [51], i.e. the averaging procedure considers the notches as an internal barrier that is shading a non-local interaction. In the case of a symmetry-axis, the material points on the other side of the symmetry axis are also considered (a mirror reflection is taken into account at the distance of 3×l_c). The objectivity of numerical results for RC structural elements within the non-local

approach was shown in [57] and [58]. The 3D calculation results within the non-local approach were demonstrated e.g. in [35], [41], [42], [67].

The characteristic length l_c is mainly determined with an inverse identification process of experimental data [59], [60]. The measured width of the localization zone in plane and reinforced concrete beams under bending was about w_{lz}≈3.5 mm (0.25 times the maximum aggregate size and 1.5 times the mean aggregate size) on the beams' surface based on the digital image correlation (DIC) results [61]. The characteristic length l_c of micro-structure should be thus assumed for concrete within isotropic elasto-plasticity and isotropic damage mechanics as about l_c=1.2-1.5 mm. i.e. l_c≈3w_{lz} [57], [60]. In order to obtain totally mesh-independent results, the element mesh size s_e should be smaller or equal to s_e=≤2×l_c [57], [60]. The numerical results of strain localization in different RC structural elements (beams, columns, walls, corbels) by using a non-local approach in softening were discussed among others in [34]-[36], [41], [42], [57], [58], [62]. The numerical results indicated that for greater l_c, the higher were both strength and ductility of concrete members. The calculations with l_c=1.2-1.5 mm would essentially lengthen the computation time. Therefore we have assumed l_c=5 mm in our FE analyses that is a limit value in order to obtain realistic results of the location and inclination of localized zones in concrete members [57].

3.2 Description of reinforcement and bond-slip law

In order to simulate the behaviour of steel bars, an elastic-perfectly plastic constitutive model was assumed with the modulus of elasticity of E_s=205 GPa and yield stress of $\sigma_y = 560$ MPa. All longitudinal bars were modelled as one-dimensional truss elements. For describing the interaction between concrete and reinforcement, a bond-slip law was defined. The interface with a zero thickness was assumed along a contact line where a relationship between the shear traction and slip was introduced. In general, this relationship is complex and depends on several factors (e.g. concrete class, concrete cover, bar diameter, bar rib height and bar rib spacing). Two different bond-failure mechanisms may appear connected to a pull-out or splitting mode. The relationship between the bond shear stress τ and slip δ followed CEB-FIP Code [63] (Fig.8). This bond-slip law describes 4 different phases by taking hardening/softening into account in the relationship . A similar bond-slip relationship was presented in [64], based on a local fracture energy approach following earlier extensive research works on the bond-slip behaviour. We assumed the following basic bond values in FE simulations: τ_{max}=10 MPa, τ_f=3 MPa,

δ_1=1 mm, δ_2=2 mm, δ_3=5 mm and α=0.2 (Fig.8), based on our pull-out tests in the concrete block with steel bars of the diameter ϕ=12 mm [34], [65] (the pull-out tests with steel bars of ϕ=20 mm were not carried out). Since the calculated bond stresses τ_b were clearly below τ_{max} (based on preliminary simulations), the effect of the bar diameter ϕ on τ_{max} was neglected, thus

$$\tau_b = \begin{cases} \tau_{max}\left(\dfrac{\delta}{\delta_1}\right)^{\alpha} & 0 < \delta \le \delta_1 \\ \tau_{max} & \delta_1 < \delta \le \delta_2 \\ \tau_{max} - \left(\tau_{max} - \tau_f\right)\dfrac{\delta - \delta_1}{\delta_3 - \delta_2} & \delta_2 < \delta \le \delta_3 \\ \tau_f & \delta_3 < \delta \end{cases}. \quad (17)$$

In addition, the calculations were carried out with the different parameters δ_1 (Fig.8) and perfect bond. The constitutive model for concrete was implemented into the commercial finite element code Abaqus [43]. The non-local averaging was performed in the current configuration. This choice was governed by the fact that element areas in this configuration were automatically calculated by Abaqus [43]. Due to the access lack to information on integration points stored internally by Abaqus, a special technique was applied to perform non-local averaging by means of the UMAT (user constitutive law definition) subroutine. Two FE-meshes with the identical topology (on the same set of nodes) were defined. The finite elements from the first mesh were first called in an iteration (they had lower labels). They gathered information about coordinates of integration points, current total strains (to calculate equivalent strains) and a volume associated with integration points. They had no stiffness and always returned a zero force vector, so they did not affect the FE results. Next the finite elements from the second mesh (with higher labels) were called. They used the information gathered by elements from the first mesh (and stored in a globally accessed Fortran variable) to calculate non-local quantities and return a stress vector.

4. Comparison between FE model responses and test results

The FE analyses were performed for experimental reinforced concrete beams under plane stress conditions. In the FE calculations, some simplifications were assumed. First, 2D calculations were carried out and the half part of beams was analyzed only (Fig.9) in order to strongly reduce the computation time. Thus, a symmetric failure mode was taken into account in contrast to the experimental results. In order to capture a statistical size effect, the full beam should be taken into account with a

statistical distribution of the concrete tensile strength using a correlated random field [65]. However, the effect of a statistical distribution of the concrete tensile strength on the location of the critical diagonal crack was insignificant [65].

In the present simulations, the 2D meshes consisting of 57,700-203,500 plane stress triangular elements with linear shape functions in the so-called 'union jack pattern' were used to avoid locking (Fig.9). The size of quadrilateral elements was very small (s_e=5 mm) and was equal to l_c=5 mm (Fig.9).

4.1 Force-displacement curves

The FE results of force-displacement curves were compared to the experiments in the plots of Fig.10 (for η_a=1-6). The experimental ultimate vertical forces were well reproduced in the FE analyses for the same failure mode (Tab.2). The maximum difference was 0.5-7.5% (Tab.2). The largest difference was for the highest beam S2D36a72_2 (η_a=2) - 7.5% (Fig.10e). Note that both the shear-tension failure and shear-compression failure might occur in the experiment for η_a=2. However, in the FE calculations, the shear-compression failure was solely reproduced for this beam. Therefore the calculated shear strength for S2D36a72_1 (η_a=2) was significantly too high (47.4%) due to the different failure mode (Fig.10e). The softening (post-peak) modulus, calculated as the inclination tangent of the force-deflection curve to the horizontal after the peak force, defined as $E_s = |\Delta F/\Delta u|$, (Fig.10) increased with decreasing parameter η_a for $\eta_a \leq 3$, from E_s=40-230 kN/mm for η_a=3 up to E_s=1400-1600 kN/mm for η_a=1-1.5.

In the numerical analyses, the mobilized bond stress τ_b between concrete and reinforcement (Eq.17, Fig.8) was located always on the hardening curve of Fig.8 below the plateau ($\tau_b < \tau_{max}$). The maximum bond stress was between 7-8 MPa (large beams) and 4-6 MPa (small beams), i.e. $< \tau_{max}$=10 MPa.

Figure 11 presents the calculated shear strength $\tau_c = V_{max}/(tD)$ ($V_{max} = 0.5F_{max}$) with increasing parameters η_a and η_l as compared to the experimental values. The calculated results were also compared with the shear strength according to our strut-and-tie model, being an improved alternative to the ACI approach [21] (the model was described in [20])

$$\tau_c = \frac{1-\eta_c}{\eta_a} \frac{\rho_l f_y [\eta_a^2 + (1-\eta_c)^2]}{\eta_a^2 + (1-\eta_c)^2 + \frac{1}{2\eta_c}\frac{\rho_l f_y}{f_c}(1-\eta_c)^2}, \quad (18)$$

where f_y - the yield stress in reinforcement.

The agreement between the numerical and experimental results is satisfactory. The effective failure stress τ_c increased with increasing depth D due to a different failure mode but decreased with increasing span ratio η_a. In the series '1', the mean experimental value was τ_c=1.34 MPa (η_a=6), τ_c=1.35 MPa (η_a=3) and τ_c=2.86 MPa (η_a=1.5) for the beams S1D18a108, S1D36a108 and S1D72a108 (the numerical values were: 1.36 MPa, 1,39 MPa and 3.15 MPa, respectively) (Fig.11). In the series '2', the measured shear strength decreased with increasing shear span a and effective length l_{eff} from τ_c=7.39 MPa (η_a=1) to τ_c=2.11 MPa (η_a=2) and next to τ_c=1.31 MPa (η_a=3) for the beams S2D36a36, S2D36a72 and S2D36a108 (the numerical values were: 7.26 MPa, 2.62 MPa and 1.39 MPa, respectively) (Fig.11). Equation 18 yielded the realistic shear strength results in the range of $\eta_a \geq 1.5$ as compared to the experimental and numerical outcomes. However, for η_a=1 it provided a too small assessment of the shear strength.

4.2 Strain localization zones

Figures 12 and 13 show the contours of the non-local equivalent strain measure $\bar{\varepsilon}$ (Eq.15) with the attached scale as compared with the experimental cracks pattern (marked as lines). The experimental critical diagonal crack was marked by the red arrow and the numerical critical diagonal localization zone was marked by the yellow arrow. For the sake of clarity, the longitudinal steel bars were removed. The calculated strain localization zones were obviously symmetric in contrast to the experimental cracks (Figs.12 and 13). However the overall characteristic of failure modes (reinforcement yielding or concrete shear mechanism) was satisfactorily reflected in calculations. The geometry of localized zones from FEM satisfactorily matched the experimental crack pattern (Figs.12 and 13), although some differences existed. In general, the differences became greater with decreasing η_a. The critical localized zone was too curved for the beam S1D36a108 (D=360 mm, η_a=3). The critical localized zone was located too close to the support for S1D36a108 (D=360 mm, η_a=3) and too far from the support for S1D72a108 (D=720 mm, η_a=1.5), S2D36a72_1 (L_{eff}=1980 mm, η_a=2) and S2D36a36 (L_{eff}=1260 mm, η_a=1).

The calculated inclination of the critical diagonal localized zone ($\eta_a \geq 2$) matched well the mean experimental crack values (Fig.14). However for $\eta_a \leq 1.5$ it was slightly too steep (47-49° against 42-43°). Note that due to 2D simulations, 3D effects (expressed by concrete spalling due to the high horizontal compressive force ($\eta_a=1$), Fig.13c) could not be modelled.

The number of localized zones in FE simulations was slightly higher than in experiments. The average spacing of calculated localized zones (main and secondary) along the beam bottom was smaller by about 9-27% as compared with the experimental average crack spacing (main and secondary) (Tab.3). The highest differences were about 27% for beam S2D36a36 (Fig.13c) and 20% for beam S1D72a108 (Fig.12c). They were caused by the fact that the assumed tensile fracture energy was too high; the smaller tensile fracture energy increased the crack spacing (see Section 5.1, Figs.18 and 19).

The experimental mean normalized height of the compressive zone at the beam top h_c/D in the shear and bending domain against η_a prior to the failure as compared to the numerical results is described in Fig.15. The agreement between experimental and numerical results is satisfactory. In the shear domain, the experimental height h_c varied from 5 cm up to 7 cm and in numerical calculations from 4.8 up to 9.2 cm. The highest difference was for $\eta_a=1$. In the bending domain, the experimental height h_c varied from 8.5 cm up to 30 cm in comparison in view of 9 cm up to 25 cm in calculations. The highest difference was for $\eta_a=1.5$.

4.3 Displacements along critical diagonal crack

The calculated surface displacements along the mid-line in the critical diagonal localization zone (Figs.16 and 17) were only qualitatively compared with the experimental crack displacements due to two facts: a) the displacements were calculated at slightly different points than the measured ones due to differences between FE analyses and experiments and b) the displacement calculations were carried out within continuum mechanics while the discrete cracks occurred in experiments (thus a direct comparison was not possible). The comparison was performed for the beam S1D36a108 (with the diagonal shear-tension failure mode) (Fig.16) and S1D72a108 (with the diagonal shear-compression failure mode) (Fig.17) for two points along the critical shear zone. In addition, the evolution of the critical crack/localization zone width along its length was presented in Fig.18 for the beams S1D36a108 and S1D72a108, based on the

results at three points along the crack length (at reinforcement, at the beam mid-height and at the upper beam part).

In the case of the beam S1D36a108 (η_a=3), the normal displacement ω along the entire critical diagonal localized zone was larger than the tangential displacement δ (Fig.16) that was consistent with our experimental outcomes [19]. For the beam S1D72A108 (η_a=1.5), the tangential crack displacement δ was higher than the normal one ω along the critical diagonal localized zone in the upper beam region (Fig.17) as in the experiments [19]. The calculated widths of the critical localization zone were smaller than the experimental widths of the critical crack for both the beams (Fig.18).

5. Parametric numerical study

5.1 Effect of different material constants of concrete

The impact of the different material constants on the behaviour of reinforced concrete beams is shown for the beam S1D36a108 (η_a=3) (Fig.19) and beam S1SD72a108 (η_a=1.5) (Fig.20). The different material constants were assumed, which controlled the damage under tension (β=60 instead of β=85), damage under compression (η_2=0.20 and δ_c=250 instead of η_2=0.15 and δ_c=150) and threshold parameter $\kappa_0=7\times10^{-5}$ (instead of $\kappa_0=9\times10^{-5}$). The remaining material constants (listed in Section 4) had a smaller impact and were kept constant. In addition, one calculation was also performed for the case when elasto-plasticty and damage were both switched off under compression. The decreasing parameter β corresponded to a slight increase of the tensile fracture energy (from G_f=100 N/m up to G_f=120 N/m). The increasing parameters η_2 and δ_c were equivalent to the decrease of the compressive strength and compressive fracture energy (from f_c=60 MPa and G_c=4000 N/m down to f_c=50 MPa and G_c=3000 N/m). The reduction of the threshold parameter κ_0 corresponded to the lower tensile strength and tensile fracture energy (from f_t=3.2 MPa and G_f=100 N/m down to f_t=2.6 MPa and G_f=80 N/m).

The impact of the tensile strength and tensile fracture energy was more pronounced for the beam S1D36a108 (η_a=3 with the diagonal tensile failure mode) than for S1D72a108 (η_a=1.5). In contrast, the impacts of the compressive strength and fracture energy were most significant for the beam S1D72a108 (η_a=1.5 with the shear compression failure mode).

For the low beam S1D36a108 (η_a=3), the maximum vertical force became larger with increasing tensile fracture energy and became smaller with decreasing compressive strength and fracture energy (Fig.19). The decreasing threshold parameter κ_0 (lower tensile strength and tensile fracture energy) lead obviously to a pronounced decrease of the ultimate vertical force (about 15%). The distance of inclined localized zones from the support increased with decreasing parameter β and increasing parameters η_2 and δ_c. In addition the localized zones became steeper. For the smaller value of κ_0 (Fig.19d), the agreement between the shape and location of the critical diagonal localized zone as compared to the experiment was better. In addition, the bending localized zones were more developed in the central beam part (Fig.19d) and their number increased with growing tensile fracture energy.

For the high beam S1D72a108 (η_a=1.5), the vertical force decreased by 20% with decreasing compressive strength and fracture energy (due to increase of the compression softening parameters η_2 and δ_c) (Fig.20). The decreasing tension softening parameter β lead to the growth of the vertical force merely by 1%. For the smaller value of κ_0, the bending localized zones were more developed in the central beam part (Fig.20d). The location of the critical diagonal localized zone was not affected by the change of material parameters. This shows that the 3D effect should be taken into account in FE analysis in order to obtain better agreement for the beams with η_a=1-1.5. When plasticity and damage were switched off in compression, the different failure modes occurred (Figs.19e and 20e). The beams' strength strongly increased. Both the beams failed due to plastic flexural mechanism that was expressed by reinforcement yielding. A large number of more developed bending localized zones were observed in the central beam portion. The curved shear localized zones did not occur. Since all stress limits for concrete were switched off in compression, the beam strength mainly depended upon the amount of steel reinforcement that was high (ρ_L=1.4%). The maximum concrete stress in the beam upper central part was strongly above the concrete compressive strength (e.g. 100 MPa for the beam S1D36a108). Thus, a huge increase of the ultimate vertical force occurred. The consideration of non-linearity in the compressive region counteracted a strong shortcoming of our constitutive model caused by an isotropic response in cracking. Our model for concrete needs the non-linearity in compression to get a more realistic shear crack response (and to improve the incorrect physics of the model).

5.2 Effect of bond-slip stiffness

In the calculations, the different slip values were assumed according to Fig.8: δ_1=0.5 mm, δ_2=1.5 mm, δ_3=4.5 mm (instead of the basis data: δ_1=1 mm, δ_2=2 mm, δ_3=5 mm) in order to investigate the effect of the bond stiffness (the first set of constants corresponds to a stiffer bond). In addition two extreme bonds were considered: 1) very weak bond (δ_1=100 mm, δ_2=200 mm, δ_3=500 mm) (Fig.8) and 2) perfect bond. The calculation results in Figs. 21 and 22 are shown for two beams: S1D36a108 (η_a=3) and S2D36a72 (η_a=2).

The ultimate vertical force P_{max} increased by about 3% (beam S1D36a108) and 5% (beam S2D36a72) with the stiffer bond (curves 'b' in Figs.21 and 22). The pattern of localized zones was very similar for the beam independently of the bond stiffness for the beam S1D36a72 with η_a=2 (Fig.21). For the beam S1D36a108 (η_a=3), the critical diagonal shear crack was moved more to the beam mid-region with the larger bond stiffness (Fig.22). The perfect bond lead to the increase of the peak load P_{max} by about 5% (beam S1D36a108) and 8% (beam S2D36a72). For both the beams more localized bending zones occurred in the beam mid-region. In contrast the very weak bond contributed to the decrease of P_{max} by 14% for the beam S1D36a108 and 5% for the beam S2D36a72. For both the beams less localized zones occurred (e.g. two localized zones merely occurred in the beam mid-region of S1D36a72).

6. Conclusions

The following basic conclusions can be derived from our FE analyses on the size effect in RC beams without stirrups which were scaled along the height or length:

- The enhanced coupled elastic-plastic-damage formulation was capable to offer good agreement with the laboratory experiments using the same set of material constants with respect to both the strength and failure modes. The material constants were calibrated by accompanying standard laboratory tests. The differences between numerical outcomes and experimental results with respect to the critical diagonal crack location grew with decreasing η_a (the numerical critical diagonal localization zone was located too far from the beam support and its inclination to the horizontal was too steep for η_a=1-1.5 as compared to the experimental outcomes). These discrepancies were due to 3D mechanical experimental effects that were not considered in 2D simulations.

- The mechanical behaviour observed in RC beams was very sensitive to the beam dimensions. The shear strength and brittleness increased with increasing effective height and decreased with increasing shear span-effective height ratio. The diagonal tension failure (wherein normal displacements were higher than tangential displacements along the critical diagonal crack) and shear compression failure (wherein normal displacements were smaller than tangential displacements along the critical diagonal crack in the top region) were realistically reproduced in calculations.

- The numerical shear strength of RC beams became higher with increasing tensile and compressive fracture energy, tensile and compressive strength and slip-bond stiffness. During the diagonal tension failure, the effect of tensile parameters was stronger and during shear compression failure, the effect of compressive parameters was more pronounced. The size effect was now related to the actual failure mechanism represented by its respective strength and energy parameters.

Acknowledgments

The research works have been carried out within the project: "*Innovative ways and effective methods of safety improvement and durability of buildings and transport infrastructure in the sustainable development*" financed by the European Union (POIG.01.01.02-10-106/09-01) and within the project: "*Experimental and numerical analysis of coupled deterministic-statistical size effect in brittle materials*" financed by the National Science Centre NCN (UMO-2013/09/B/ST8/03598).

The numerical calculations were performed on supercomputers of the Academic Computer Centre in Gdańsk TASK.

References

[1] Z.P. Bažant, J. Planas, *Fracture and size effect in concrete and other quasi-brittle materials.* CRC Press LCC; 1989.

[2] A. Carpinteri, Decrease of apparent tensile and bending strength with specimen size: two different explanations based on fracture mechanics, *Int. J. Solids Struct*. 25(4) (1989) 407-29.

[3] K. Duan, Z. Hu, Specimen boundary induced size effect on quasi-brittle fracture, *Strength Fract. Complexity* 2(2) (2004) 47-68.

[4] Z.P. Bažant, S.D. Pang, M. Vorechovsky, S. Novak, Energetic-statistical size effect simulated by S6FEM with stratified sampling and crack band model, *Int. J. for Numerical Methods in Engineering* 71(11) (2007) 1297-1320.

679 [5] J.C. Walraven, *The influence of depth on the shear strength of lightweight concrete beams without*
680 *shear reinforcement*, Stevin Laboratory Report No.5-78-4, Delft University of Technology, vol. 36
681 (1978).
682 [6] Z.P. Bažant, M.T. Kazemi, Size effect on diagonal shear failure of beams without stirrups, *ACI Struct*
683 *J* 88(3) (1991) 268-76.
684 [7] J.K. Kim, Y.D. Park, Shear strength of reinforced high-strength concrete beams without web
685 reinforcement, *Mag Concr Res* 46(166) (1994) 7-16.
686 [8] K.H. Tan, H.Y. Lu, Shear behaviour of large reinforced concrete deep beams and code comparisons,
687 *ACI Struct J* 96(5) (1999) 836–45.
688 [9] D. Angelakos, E.C. Bentz, M.P. Collins, Effect of concrete strength and minimum stirrups on shear
689 strength of large members, *ACI Struct J* 98(3) (2001) 290-300.
690 [10] K.H. Yang, H.S. Chung, H.C Eun, Shear characteristics of high-strength concrete deep beams
691 without shear reinforcements, *Eng Struct* 25(10) (2003) 1343-52.
692 [11] K.H. Reineck, D. Kuchma, K.A. Kim, S. Marx, Shear database for reinforced concrete members
693 without shear reinforcement, *ACI Struct J* 100(2) (2003).
694 [12] A. Lubell, T. Sherwood, E. Bentz, M. Collins, Safe shear design of large, wide beams, *Concr Int*
695 26(1) (2004) 66-78.
696 [13] K.H. Tan, G.H. Cheng, H.K. Cheong, Size effect in shear strength of large beams-behaviour and
697 finite element modelling, *Mag Concrete Res* 57(8) (2005) 497-509.
698 [14] E. Syroka-Korol, J. Tejchman, Experimental investigations of size effect in reinforced concrete
699 beams failing by shear. Engineering Structures 58 (2014) 63-78.
700 [15] J.C. Walraven, N. Lehwalter, Size effects in short beams loaded in shear, *ACI Struct J* 91(5) (1994)
701 585-93.
702 [16] N. Zhang, K.H. Tan, Size effect in RC deep beams: Experimental investigation and STM
703 verification, *Eng Struct* 29 (2007) 3241-54.
704 [17] C.M. Belgin, S. Şener, Size effect on failure of overreinforced concrete beams, *Eng Fract Mech*
705 75(8) (2008) 2308-19.
6 [18] C. Carpintieri, J.R Carmona, G. Ventura, Failure mode transitions in reinforced concrete beams. Part
7 2: Experimental tests, *ACI Struct J* 108 (2011) 286-93.
8 [19] M. Słowik, P. Smarzewski, Study of the scale effect on diagonal crack propagation in concrete
9 beams, *Comput Mater Sci* 64 (2012) 216-220.
0 [20] J. Suchorzewski, E. Korol, J. Tejchman, Z. Mroz, Experimental study of shear strength and failure
1 mechanisms in RC beams scaled along height or length, *Engineering Structures* 157 (2018) 203-223.

712 [21] ACI 318-14: Building code requirements for structural concrete, American Concrete Institute, 2014.
713 [22] N. Zhang, K. Tan, Direct strut-and-tie model for single span and continuous deep beams, *Eng.*
714 *Structures* 29 (2007) 2987-3001.
715 [23] D. Krajcinovic, G. Fonseka, The continuous damage theory of brittle materials, *Journal of Applied*
716 *Mechanics ASME* 48 (4) (1981) 809-824.
717 [24] J. Mazars, A description of micro- and macroscale damage of concrete structures, *Engineering*
718 *Fracture Mechanics* 25(5-6) (1986) 729-737.
719 [25] J.C. Simo, J. Ju, Strain- and stress-based continuum damage models, *International Journal for Solids*
720 *and Structures* 23(7) (1987) 821-840.
721 [26] J. Lubliner, J. Oliver, S.E. Oller, E. Onate, A plastic-damage model for concrete, *International Jour-*
722 *nal of Solids and Structures*, 25(3) (1989) 299-326.
723 [27] G. Meschke, R. Lackner, H.A. Mang, An anisotropic elastoplastic-damage model for plain concrete,
724 *Int. J. for Numerical Methods in Engineering* 42(4) (1998) 702-727.
725 [28] R. Faria, J. Oliver, M. Cervera, A strain-based plastic viscous-damage model for massive concrete
726 structures, *International Journal of Solids and Structures* 35(14) (1998) 1533-1558.
727 [29] E. Hansen, K. Willam, A two-surface anisotropic damage-plasticity model for plane concrete, *Pro-*
728 *ceedings Int. Conf. Fracture Mechanics of Concrete Materials*, R. de Borst [Ed.], Paris, Balkema, 549–
729 556, 2001.
730 [30] J.F. Chen, E.V. Morozov, K. Shankar, A combined elastoplastic damage model for progressive fail-
731 ure analysis of composite materials and structures, *Composite Structures* 94 (2012) 3478-3489.
732 [31] P. Grassl, D. Xenos, U. Nyström, R. Rempling, K. Gylltoft, CDPM2: A damage-plasticity approach
733 to modelling the failure of concrete. *International Journal of Solids and Structures*, 50 (2013) 3805-
734 3816.
735 [32] J. Mihai, A. Jefferson, L. Lyons, Plastic-damage constitutive model for the finite element analysis
736 of fibre reinforced concrete, *Engineering Fracture Mechanics* 159 (2016) 35-62.
737 [33] G. Xotta, S. Beizaee, K.J. Willam, Bifurcation investigations of coupled damage-plasticity models
738 for concrete materials, *Computer Methods in Applied Mechanics and Engineering* 298 (2016) 428-452.
9 [34] E. Korol, J. Tejchman, Z. Mroz, Experimental and numerical assessment of size effect in
0 geometrically similar slender concrete beams with basalt reinforcement, *Engineering Structures* 141
1 (2017) 272-291.
2 [35] I. Marzec, L. Skarżyński, J. Bobiński, J. Tejchman, Modelling reinforced concrete beams under
3 mixed shear-tension failure with different continuous FE approaches, *Computers and Concrete* 12(5)
4 (2013) 585-612.

[36] L. Skarżyński, I. Marzec, J. Tejchman, Experiments and numerical analyses for composite RC-EPS slabs, *Computers and Concrete* 20(6) (2017) 689-704.

[37] I. Marzec, J. Tejchman, Enhanced coupled elasto-plastic-damage models to describe concrete behaviour in cyclic laboratory tests: comparison and improvement, *Archives of Mechanics* 64(3) (2012) 227-259.

[38] I. Marzec, J. Tejchman, Computational modelling of concrete behaviour under static and dynamic conditions, *Bulletin of the Polish Academy of Sciences - Technical Science*s 61(1) (2013) 85-96.

[39] I. Marzec, J. Tejchman, A. Winnicki, Computational simulations of concrete behaviour under dynamic conditions using elasto-visco-plastic model with non-local softening, *Computers and Concrete* 15(4) (2015) 515-545.

[40] J. Pamin, R. de Borst, Stiffness degradation in gradient-dependent coupled damage-plasticity. *Archives of Mechanics* 51, 3-4 (1999) 419-446.

[41] T. Majewski, J. Bobinski, J. Tejchman, FE-analysis of failure behaviour of reinforced concrete columns under eccentric compression, *Engineering Structures* 30(2) (2008) 300-317.

[42] T. Malecki, T. Marzec, J. Bobiński, J. Tejchman, Effect of a characteristic length on crack spacing in a reinforced concrete bar under tension, *Mechanics Research Communications* 34(5-6) (2007) 460-465.

[43] Abaqus documentation, Version 6.13; 2013.

[44] R.H.J. Peerlings, R. de Borst, W.A.M. Brekelmans, M.G.D., Geers, Gradient enhanced damage modelling of concrete fracture. *Mechanics of Cohesive-Frictional Materials* 3 (1998) 323-342.

[45] M.G.D. Geers, Experimental analysis and computational modeling of damage and fracture, *PhD Thesis*, Eindhoven University of Technology, 1997.

[46] J. Lee, G.L. Fenves, Plastic-damage model for cyclic loading of concrete structures. *Journal of Engineering Mechanics* 124(8) (1998) 892-900.

[47] I. Carol, K. Willam, Spurious energy dissipation/generation in stiffness recovery models for elastic degradation and damage, *International Journal Solids Structures,* 33(20-22), (1996) 2939-2957.

[48] D. Karsan, J. O. Jirsa, Behavior of concrete under compressive loadings, *J. Struct. Div. ASCE* 95(12) (1969) 2543-2563.

[49] D. A. Hordijk, Local approach to fatigue of concrete, *PhD Thesis*, Delft University of Technology, 1991.

[50] G. Pijauder-Cabot, Z.P. Bažant, Non-local damage theory, *ASCE Journal of Engineering Mechanics* 113 (1987) 1512-1533.

[51] Z.P. Bažant, M. Jiràsek, Non-local integral formulations of plasticity and damage: survey of progress, *Journal of Engineering Mechanics* 128 (2002) 1119-1149.

[52] J. Bobiński, J. Tejchman, Numerical simulations of localization of deformation in quasi-brittle materials within non-local softening plasticity, *Computers and Concrete* 1(4) (2004) 1-22.

[53] J. Bobiński, J. Tejchman, Comparison of continuous and discontinuous constitutive models to simulate concrete behaviour under mixed mode failure conditions, *Int. J. Num. Anal. Meths Geom.* 40 (2016) 406-435.

[54] G. Borino, B. Failla, F. Parrinello, A symmetric formulation for non-local damage models, In Mang HA, Rammerstorfer FG, Eberhardsteiner J. (eds). *Proc. of 5th World Congress on Computational Mechanics* (WCCM V), Vienna, Austria, 2002. Vienna University of Technology. ISBN 3-9501554-0-6, http://wccm.tuwien.ac.at.

[55] P. Grassl, D. Xenos, M. Jirásek, M. Horák, Evaluation of nonlocal approaches for modelling fracture near nonconvex boundaries. *Int. J. Solids Struct*., 51 (2014) 3239-51.

[56] P. Havlásek P., Grassl, M. Jirásek, Analysis of size effect on strength of quasi-brittle materials using integral-type nonlocal models, *Engineering Fracture Mechanics* (2016) 72–85.

[57] J. Tejchman, J. Bobiński, *Continuous and discontinuous modeling of fracture in concrete using FEM.* Springer, Berlin-Heidelberg (eds. W. Wu and R. I. Borja), 2013.

[58] D. Xenos, P. Grassl, Modelling the failure of reinforced concrete with nonlocal and crack band approaches using the damage-plasticity model CDPM. *Finite Elements in Analysis and Design* 117-118 (2016) 11-20.

[59] R. Mahnken, E. Kuhl. Parameter identification of gradient enhanced damage models, *European Journal of Mechanics A/Solids,* 18 (1999) 819-835.

[60] L. Skarżyński, E. Syroka, J. Tejchman, Measurements and calculations of the width of fracture process zones on the surface of notched concrete beams, *Strain* 47 (2011) 319-332.

[61] L. Skarżyński, J. Tejchman, Experimental investigations of fracture process in plain and reinforced concrete beams under bending, *Strain* 49, 6 (2013) 521-543.

[62] E. Syroka, J. Bobiński, J. Tejchman, FE analysis of reinforced concrete corbels with enhanced continuum models. *Finite Element Methods in Analysis and Design* 47, 9 (2011) 1066-1078.

[63] CEB-FIP, CEB-FIP model code 1990, 1993.

[64] S. Yang, Y. Chen, D. Du, G. Fan, Determination of boundary effect on shear fracture energy at steel bar–concrete interface. *Engineering Fracture Mechanics* 153 (2016) 319-330.

[65] E. Syroka-Korol, J. Tejchman, Experimental investigations of size effect in reinforced concrete beams failing by shear. *Eng Struct* 58 (2014) 63-78.

[66] E. Korol, J. Tejchman, Z. Mróz, FE analysis of size effects in reinforced concrete beams without shear reinforcement based on stochastic elasto-plasticity with non-local softening, *Finite Elements in Analysis and Design* 1 (2014) 25-41.

LIST OF FIGURES

Fig.8: Bond stress-slip relationship τ_b=f(δ) by CEB-FIP [63] (Eq.17) with different parameters δ_i

Fig.9: Boundary conditions and FE mesh for RC beams (diameter of small yellow circle is related to characteristic length l_c and diameter of larger yellow circle is related to influence range of non-locality $3l_c$)

Fig.10: Experimental and calculated force-deflection F=f(u) diagrams for beams: a) S1D18a108 (D=180 mm, L_{eff}=2700 mm, a=1080 mm, η_l=15, η_a=6), b) S1D36a108 and S2D36a108 (D=360 mm, L_{eff}=2700 mm, a=1080 mm, η_l=7.5, η_a=3), c) S1D72a108 (D=720 mm, L_{eff}=2700 mm, a=1080 mm, η_l=3.75, η_a=1.5), d) S2D36a36 (D=360 mm, L_{eff}=1260 mm, a=360 mm, η_l=3.75, η_a=1) and e) S2D36a72 (D=360 mm, L_{eff}=1980 mm, a=720 mm, η_l=5.5, η_a=2)

Fig.11: Shear strength τ_c from experiments, calculations and Eq.18: a) for varying shear span parameter η_a=a/D and b) for varying length parameter η_l=l_{eff}/D (note that beams S1D18a108 for η_a=6 failed in flexural mechanism)

Fig.12: Contours of non-local equivalent strain measure $\bar{\varepsilon}$ with attached scale as compared with experimental cracks pattern for beams of series I (L_{eff}=2700 mm): a) S1D18a108 (D=180 mm, a=1080 mm, η_l=15, η_a=6), b) S1D36a108 (D=360 mm, a=1080 mm, η_l=7.5, η_a=3) and c) S1D72a108 (D=720 mm, a=1080 mm, η_l=3.75, η_a=1.5) (experimental critical diagonal crack is marked by red arrow, numerical critical localization zone is marked by yellow arrow, note that beams are not proportionally scaled and steel bars are not shown)

Fig.13: Contours of non-local equivalent strain measure $\bar{\varepsilon}$ with attached scale as compared with experimental cracks pattern for beams (D=360 mm): a) S2D36a72_1 and b) S2D36a72_2 (L_{eff}=1980 mm, a=720 mm, η_l=5.5, η_a=2) and c) S2D36a36 (L_{eff}=1260 mm, a=360 mm, η_l=3.75, η_a=1) (experimental critical diagonal crack is marked by red arrow, numerical critical diagonal localization zone is marked by yellow arrow, note that beams are not proportionally scaled and steel bars are not shown)

Fig.14: Diagonal failure crack/localized zone inclination ϕ to horizontal in RC beams for experimental series '1' (S1, square markers) and '2' (S2, triangle markers) versus ratio η_a as compared with FEM

Fig.15: Experimental and calculated normalized height of compressive zone above shear and bending crack/localized zone for varying shear span parameter $\eta_a=a/D$ (S1 - experimental series '1', S2 - experimental series '2', note that beams for $\eta_a=6$ failed in flexural mechanism)

Fig.16: Calculated evolution of normal and tangential displacements at critical diagonal localization zone from FEM for beam S1D36a108 ($\eta_a=3$) as compared to experiments: a) locations (marked by yellow arrows) and b) vertical force versus displacements: ω - normal displacement, δ - tangential displacement (experimental critical diagonal crack is marked by red arrow)

Fig.17: Calculated evolution of normal and tangential displacements at critical diagonal localization zone from FEM for beam S1D72a108 ($\eta_a=1.5$) as compared to experiments: a) locations (marked by yellow arrows) and b) vertical force versus displacements: ω - normal displacement, δ - tangential displacement (experimental critical diagonal crack is marked by red arrow)

Fig.18: Comparison between calculated (left side) and experimental (right side) normal displacements ω along normalized critical diagonal crack/localization zone length l_{exp}/l_{FEM} for: a) beam S1D36a108 and b) beam S1D72a108 (horizontal coordinate 0 - point above reinforcement (point '1' in Figs.16 and 17) and horizontal coordinate 1 - point in upper beam region (point '3' in Figs.16 and 17)).

Fig.19: Calculated force-deflection curves and distributions of non-local equivalent strain measure from FE analyses using coupled elasto-plastic-damage with non-local softening as compared to experiments (beam S1D36a108, $\eta_a=3$): a) with basis set of material constants in Section 4, b) with softening constant $\beta=60$ (instead of $\beta=85$), c) with softening constants $\eta_2=0.20$ and $\delta_c=250$ (instead of $\eta_2=0.15$ and $\delta_c=150$) d) with $\kappa_0=7\times10^{-5}$ (instead of $\kappa_0=9\times10^{-5}$) and e) without plasticity and damage under compression

Fig.20: Calculated force-deflection curves and distributions of non-local equivalent strain measure from FE analyses using coupled elasto-plastic-damage with non-local softening as compared to experiments (beam S1D72a108, $\eta_a=1.5$): a) with basis set of material constants in Section 4, b) with softening constant $\beta=60$ (instead of $\beta=85$), c) with softening constants $\eta_2=0.20$ and $\delta_c=250$ (instead of $\eta_2=0.15$ and $\delta_c=150$), d) with $\kappa_0=7\times10^{-5}$ (instead of $\kappa_0=9\times10^{-5}$) and e) without plasticity and damage under compression

Fig.21: Calculated force-deflection curves (dotted line - experiments) and distributions of non-local equivalent strain measure from FE analyses using coupled elasto-plastic-damage with non-local softening as compared to experiments (beam S2D36a72, η_a=2) for bond-slip model of Fig.8: a) Eq.17 with δ_1=1 mm, δ_2=2 mm, and δ_3=5 mm (basic data), b) Eq.17 with δ_1=0.5 mm, δ_2=1.5 mm and δ_3=4.5 mm, c) Eq.17 with δ_1=100 mm, δ_2=200 mm and δ_3=500 mm and d) perfect bond model

Fig.22: Calculated force-deflection curves (dotted line - experiments) and distributions of non-local equivalent strain measure from FE analyses using coupled elasto-plastic-damage with non-local softening as compared to experiments (beam S1D36a108, η_a=3) for bond-slip model of Fig.8: a) Eq.17 with δ_1=1 mm, δ_2=2 mm, and δ_3=5 mm (basic data), b) Eq.17 with δ_1=0.5 mm, δ_2=1.5 mm and δ_3=4.5 mm, c) Eq.17 with δ_1=100 mm, δ_2=200 mm and δ_3=500 mm and d) perfect bond model

LIST OF FIGURES

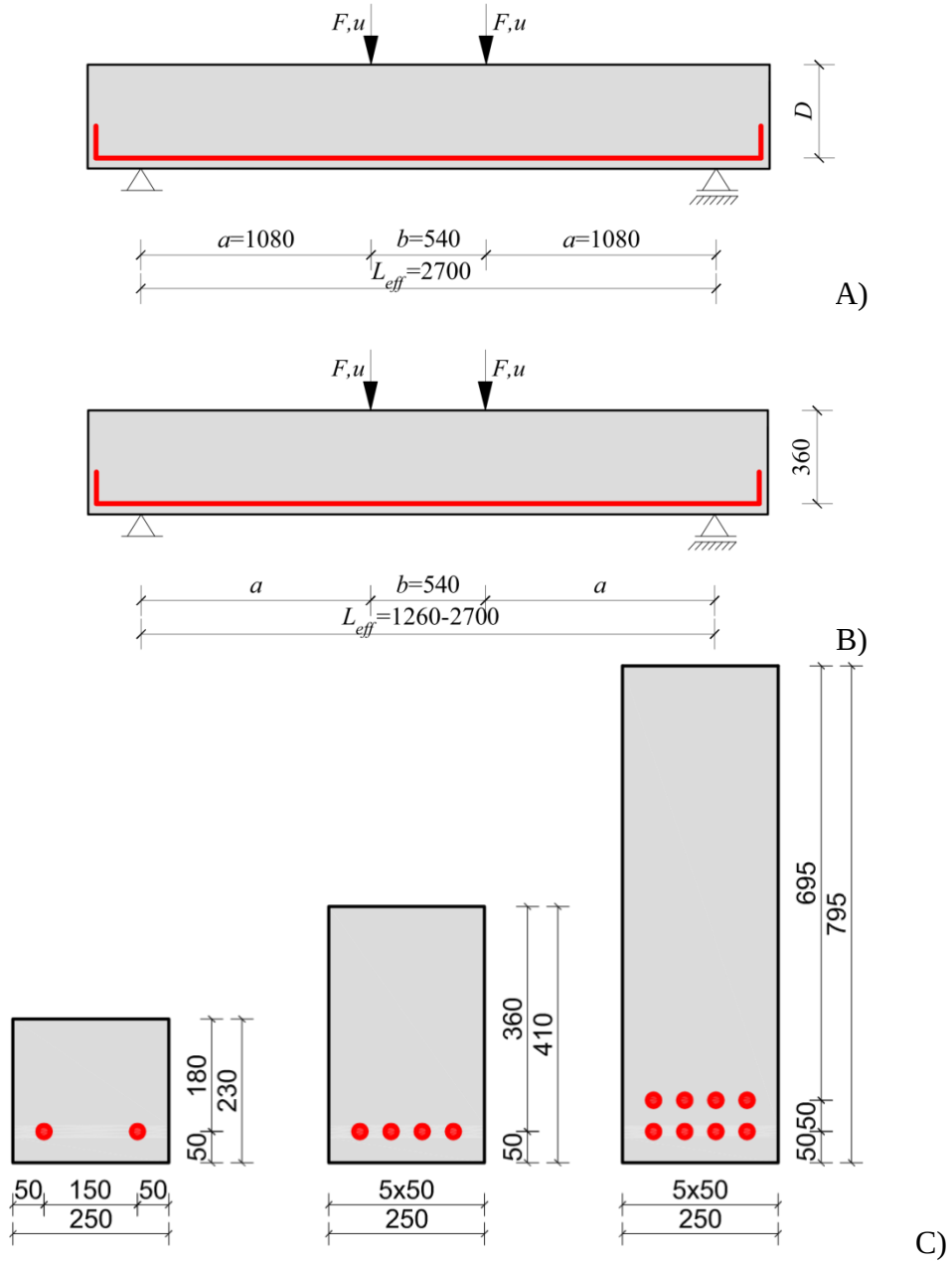

Fig.1: Experimental reinforced concrete beams under four-point bending: A) loading scheme for series '1', B) loading scheme for series '2' and C) cross-section of: a) beam S1D18a108, b) beams: S1D36a108, S2D36a36, S2D36a72, S2D36a108 and c) beam S1D72a108 [20]

FIGURE 1

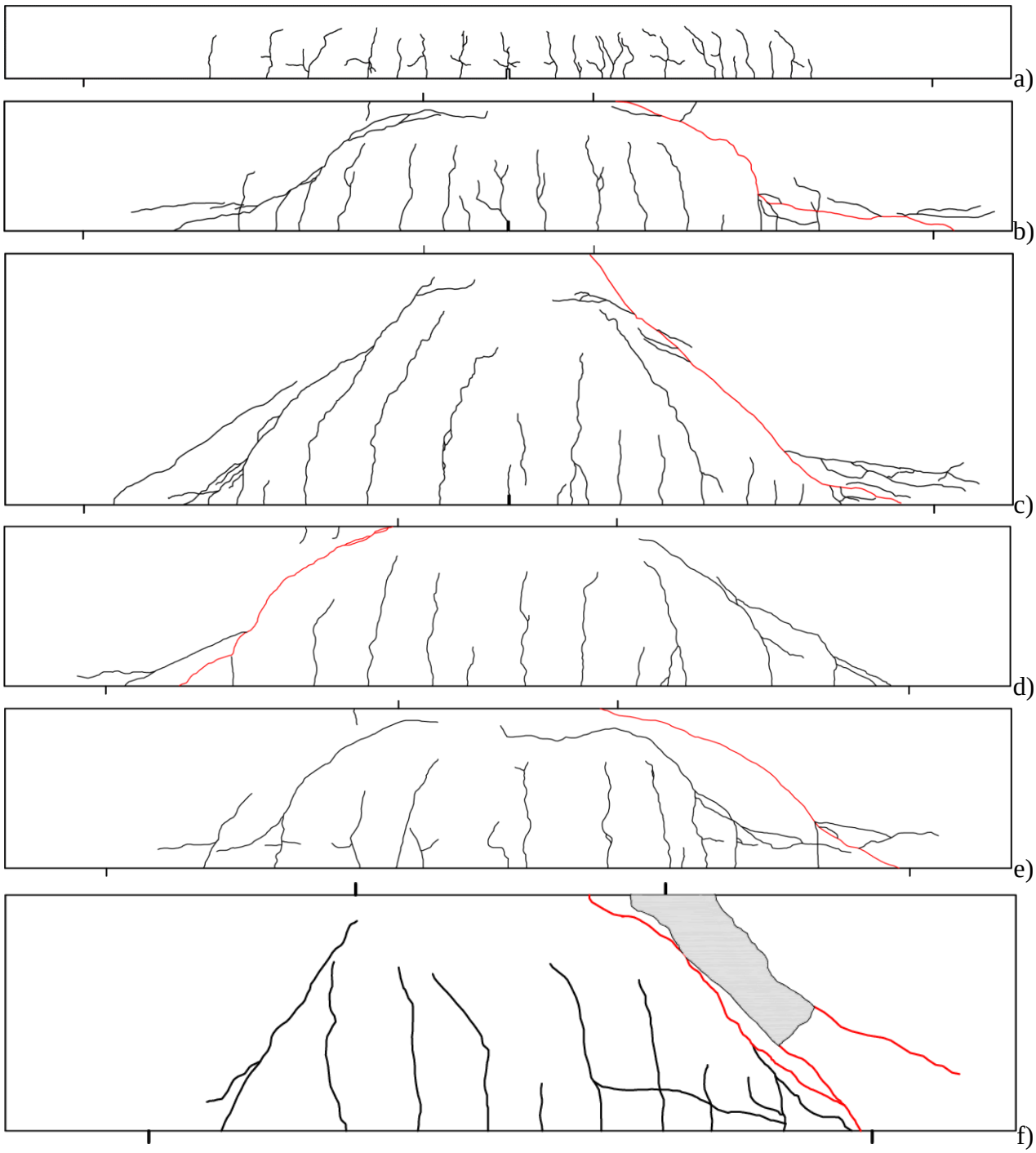

Fig.2: Crack pattern at failure typical for each beam geometry depending upon ratio *a/D* for different failure mode: a) reinforcement yielding (η_a=6), b) shear failure mode in concrete (diagonal tension) with (η_a=3), c) shear failure in concrete (diagonal shear-compression) (η_a=1.5), d) shear failure in concrete (diagonal tension) (η_a=2), e) shear failure in concrete (diagonal shear-compression) (η_a=2) and f) shear failure in concrete (diagonal shear-compression) (η_a=1) (critical diagonal crack marked in red, beams are not proportionally scaled) [20]

FIGURE 2

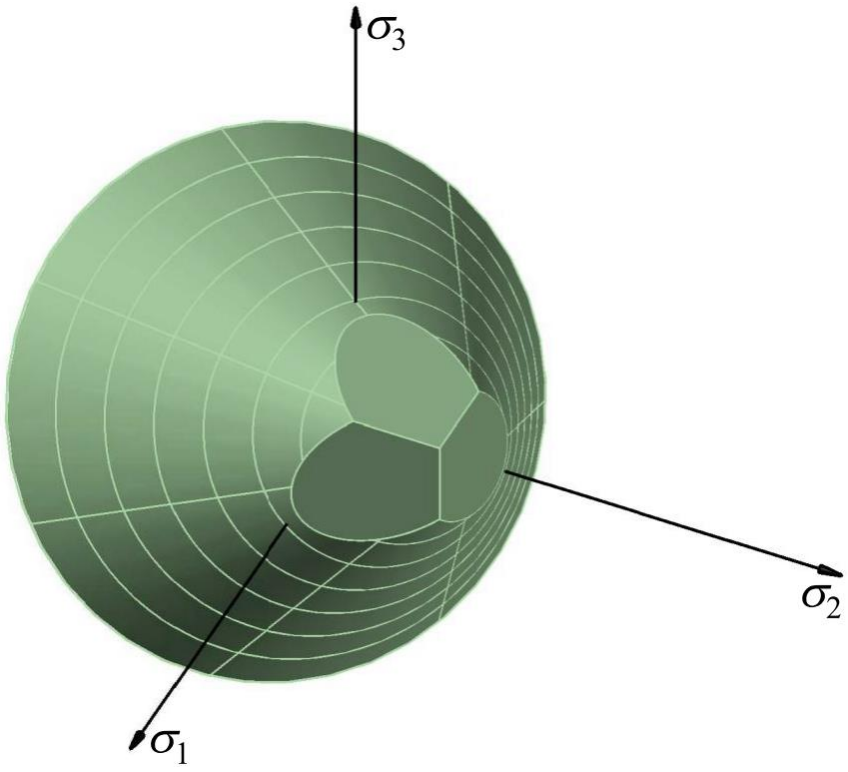

Fig.3: Failure surface of coupled Drucker-Prager-Rankine criterion for concrete in space of principal stresses

FIGURE 3

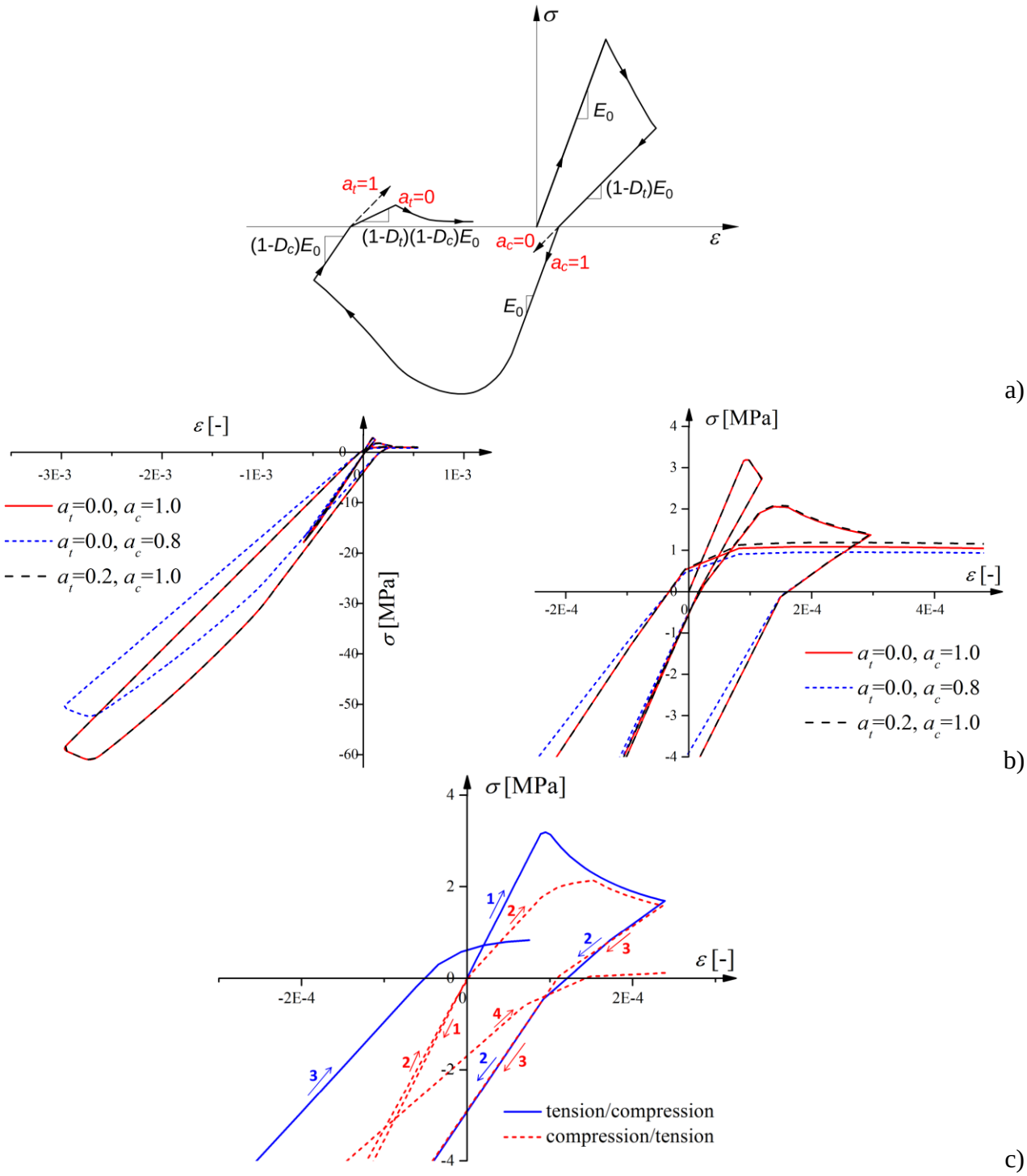

Fig.4: Uniaxial response (stress-strain σ-ε curve) of coupled elasto-plastic-damage model under cyclic loading: a) stiffness recovery concept with different damage scale factors a_t and a_c, b) influence of different damage splitting factors a_t and a_c and c) influence of load sequence (tension/compression or compression/tension) with damage splitting factors a_t=0.2 and a_c=0.8)

FIGURE 4

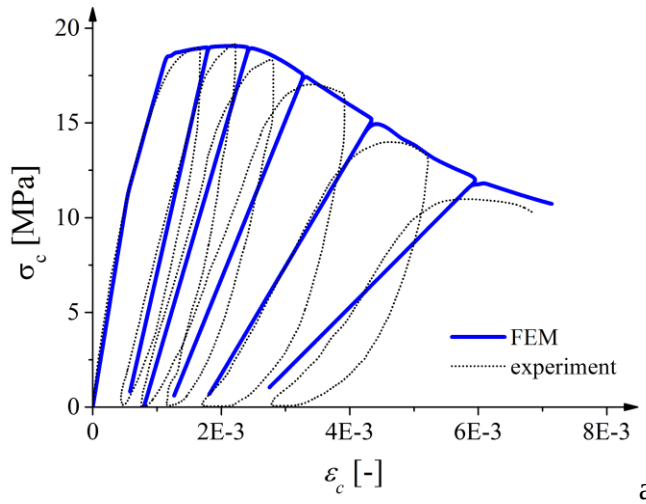

a)

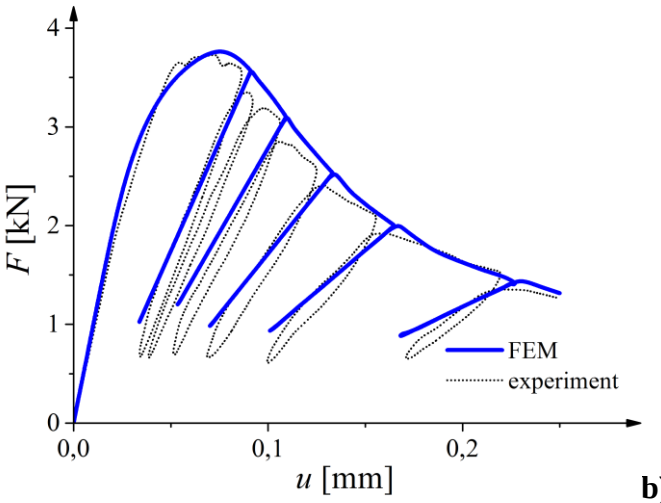

b)

Fig.5: Response of coupled elasto-plastic-damage model during uniaxial cyclic tests as compared with experimental data: a) for concrete specimen under uniaxial cyclic compression (experimental stress-strain curve by Karsan and Jirsa [48]) and b) for concrete beam under four-point cyclic bending under tensile failure (experimental force-displacement curve by Hordijk [49]) [37]

FIGURE 5

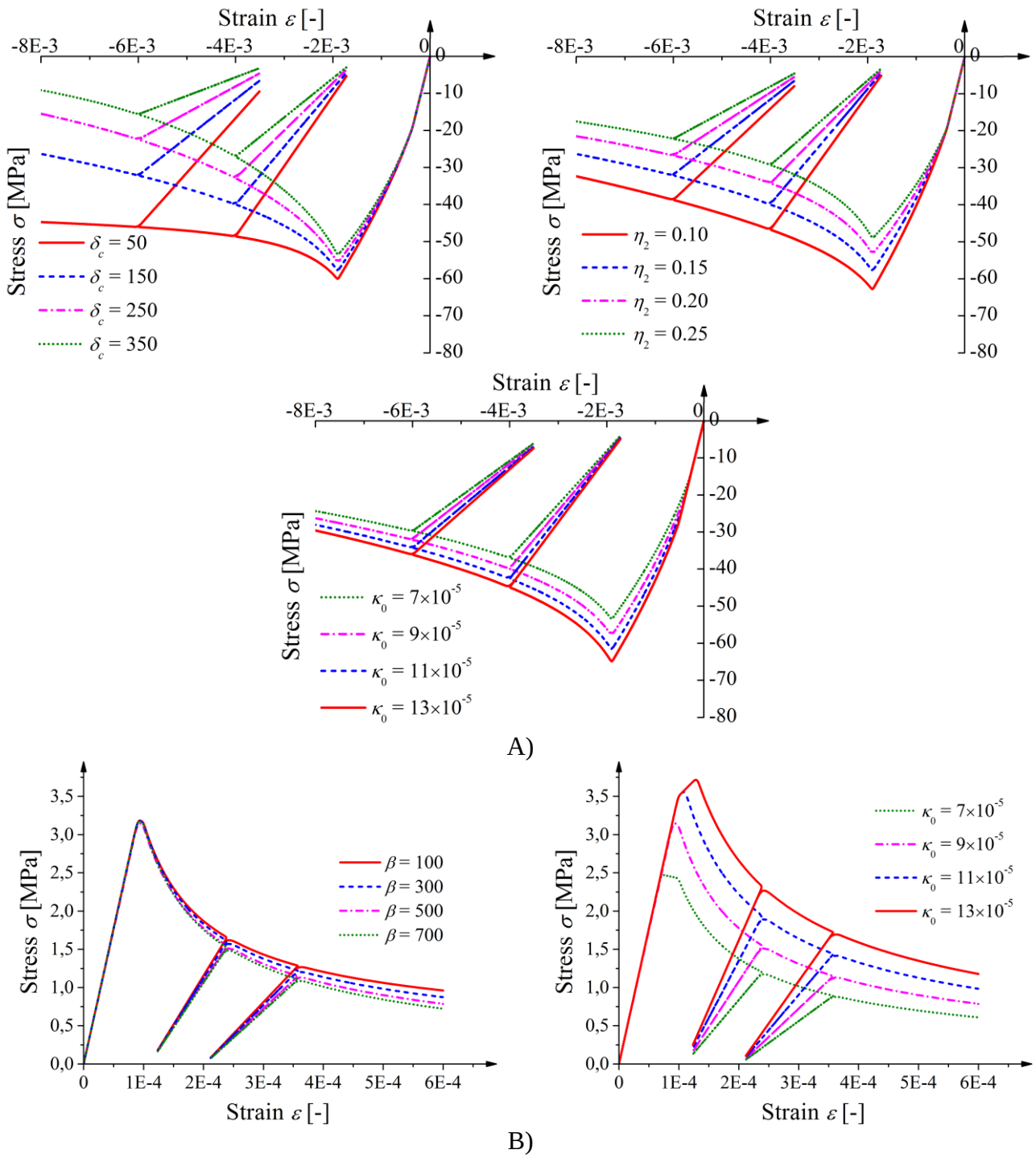

Fig.6: Effect of different material constants on uniaxial cyclic response of coupled elasto-plastic-damage model under: A) cyclic uniaxial compression and B) cyclic uniaxial tension

FIGURE 6

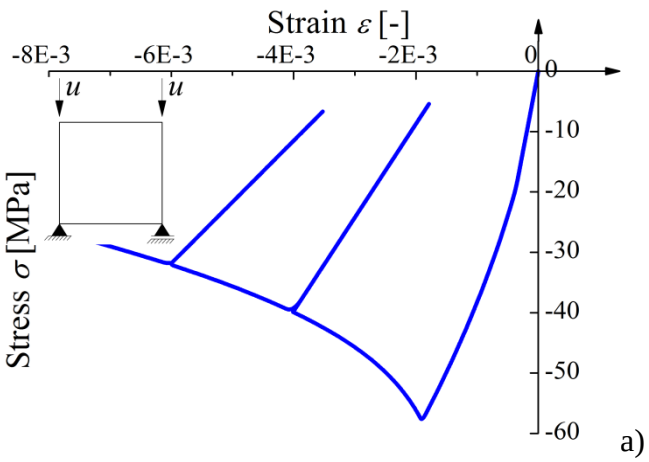

a)

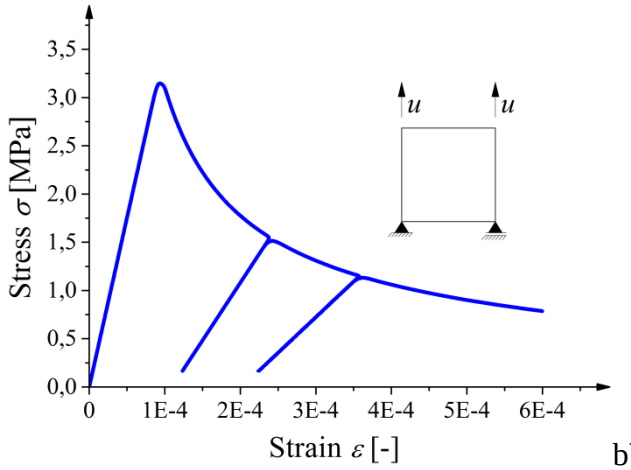

b)

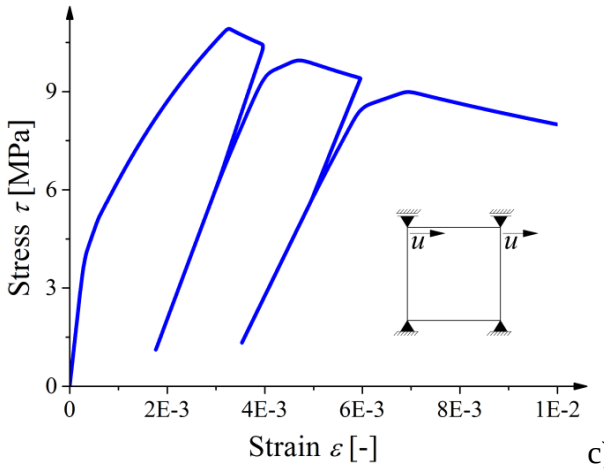

c)

Fig.7: Stress-strain curves for concrete from element tests using elasto-plastic-damage model: a) cyclic uniaxial compression, b) cyclic uniaxial tension and c) cyclic simple shear

FIGURE 7

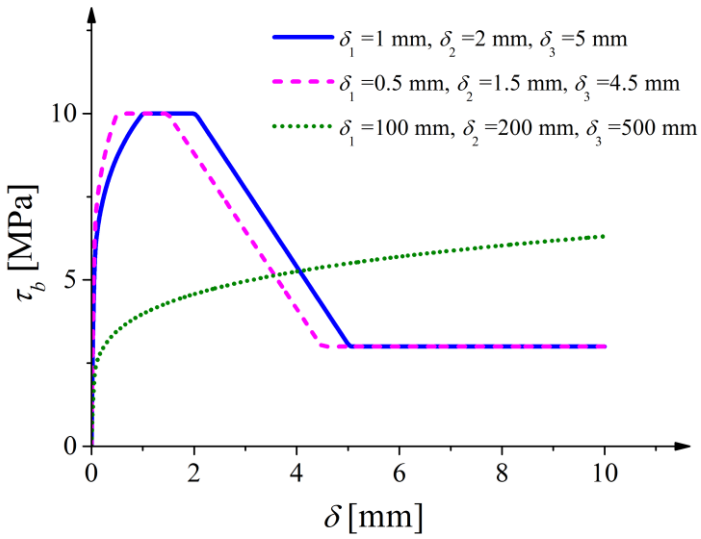

Fig.8: Bond stress-slip relationship τ_b=f(δ) by CEB-FIP [63] (Eq.17) with different parameters δ_i

FIGURE 8

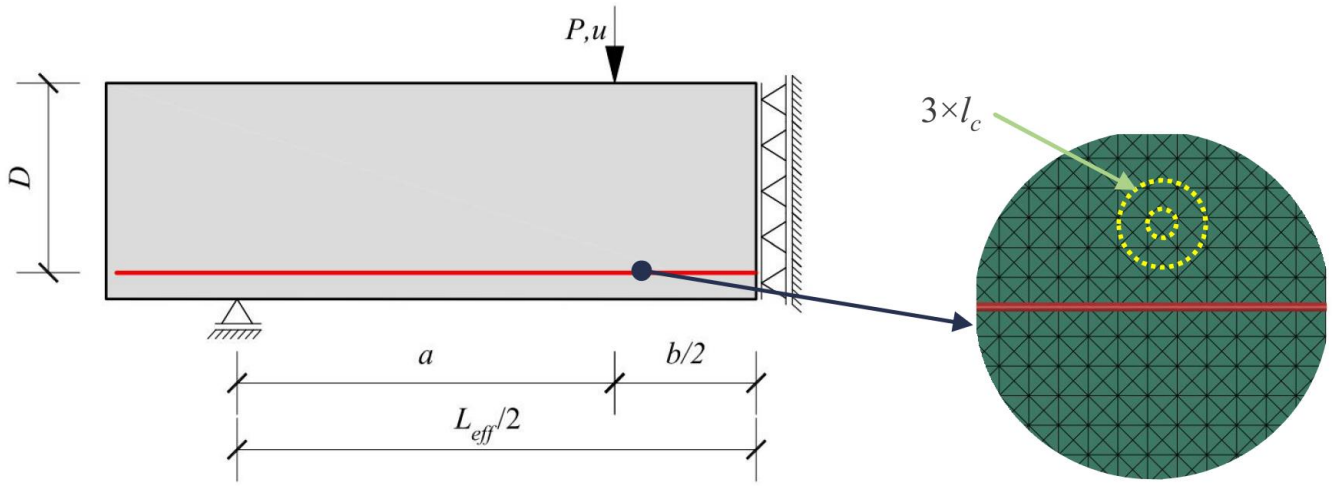

Fig.9: Boundary conditions and FE mesh for RC beams (diameter of small yellow circle is related to characteristic length l_c and diameter of larger yellow circle is related to influence range of non-locality $3l_c$)

FIGURE 9

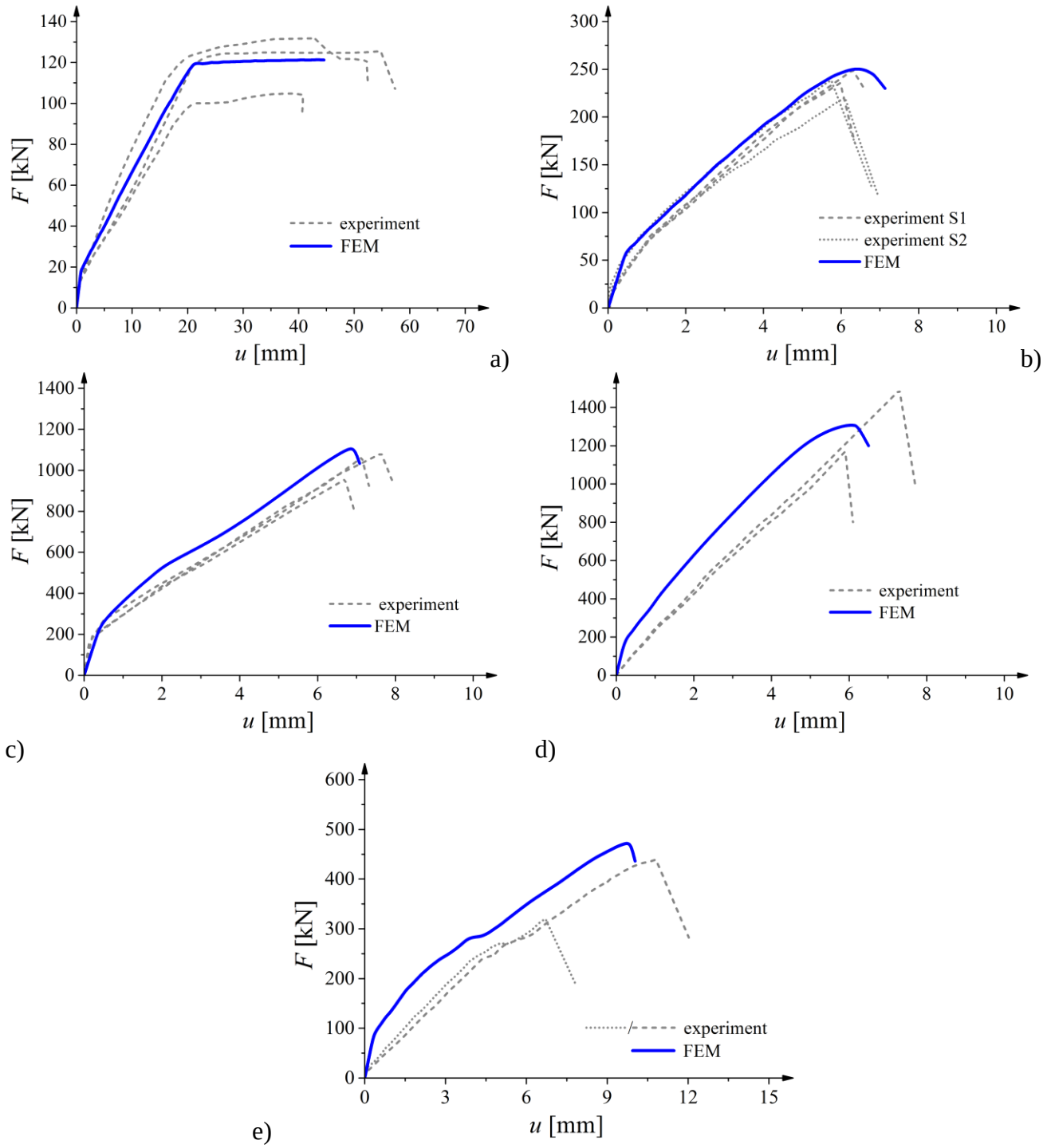

Fig.10: Experimental and calculated force-deflection F=f(u) diagrams for beams: a) S1D18a108 (D=180 mm, L_{eff}=2700 mm, a=1080 mm, η_l=15, η_a=6), b) S1D36a108 and S2D36a108 (D=360 mm, L_{eff}=2700 mm, a=1080 mm, η_l=7.5, η_a=3), c) S1D72a108 (D=720 mm, L_{eff}=2700 mm, a=1080 mm, η_l=3.75, η_a=1.5), d) S2D36a36 (D=360 mm, L_{eff}=1260 mm, a=360 mm, η_l=3.75, η_a=1) and e) S2D36a72 (D=360 mm, L_{eff}=1980 mm, a=720 mm, η_l=5.5, η_a=2)

FIGURE 10

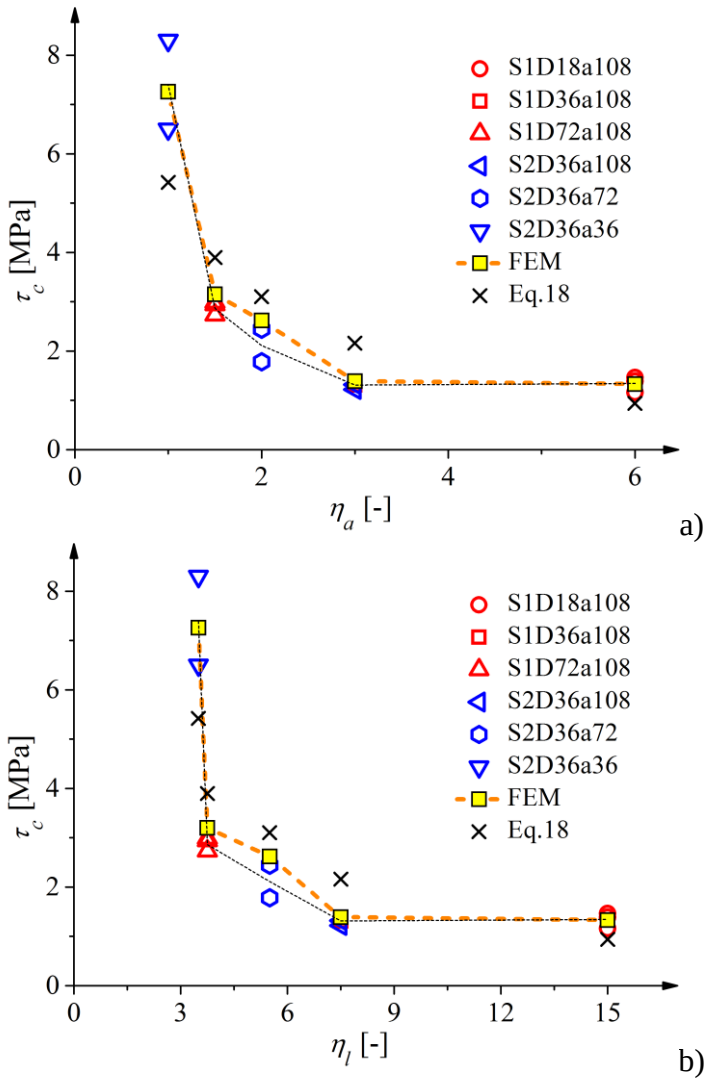

Fig.11: Shear strength τ_c from experiments, calculations and Eq.18: a) for varying shear span parameter $\eta_a=a/D$ and b) for varying length parameter $\eta_l=l_{eff}/D$ (note that beams S1D18a108 for $\eta_a=6$ failed in flexural mechanism)

FIGURE 11

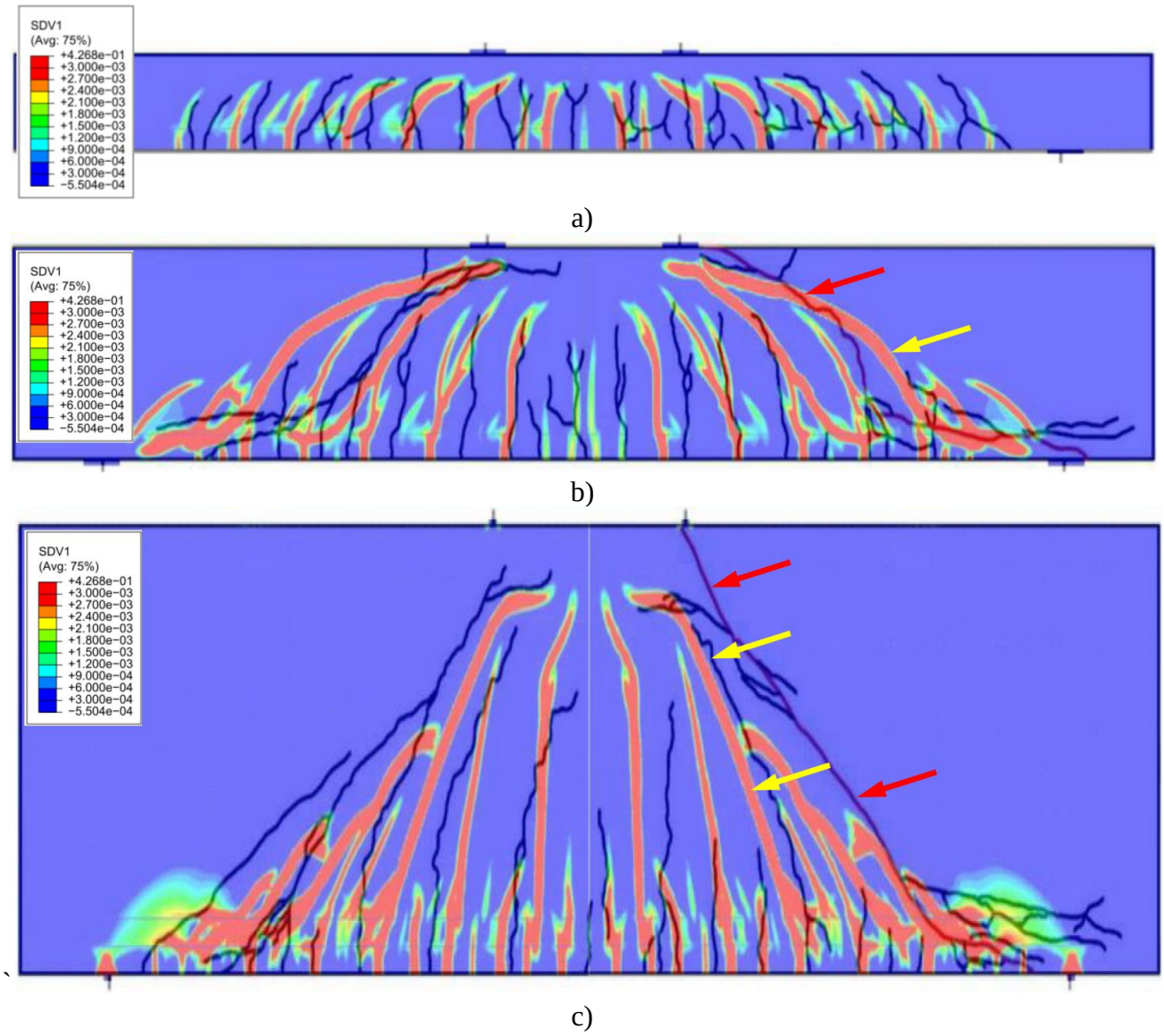

Fig.12: Contours of non-local equivalent strain measure $\bar{\varepsilon}$ with attached scale as compared with experimental cracks pattern for beams of series I (L_{eff}=2700 mm): a) S1D18a108 (D=180 mm, a=1080 mm, η_l=15, η_a=6), b) S1D36a108 (D=360 mm, a=1080 mm, η_l=7.5, η_a=3) and c) S1D72a108 (D=720 mm, a=1080 mm, η_l=3.75, η_a=1.5) (experimental critical diagonal crack is marked by red arrow, numerical critical localization zone is marked by yellow arrow, note that beams are not proportionally scaled and steel bars are not shown)

FIGURE 12

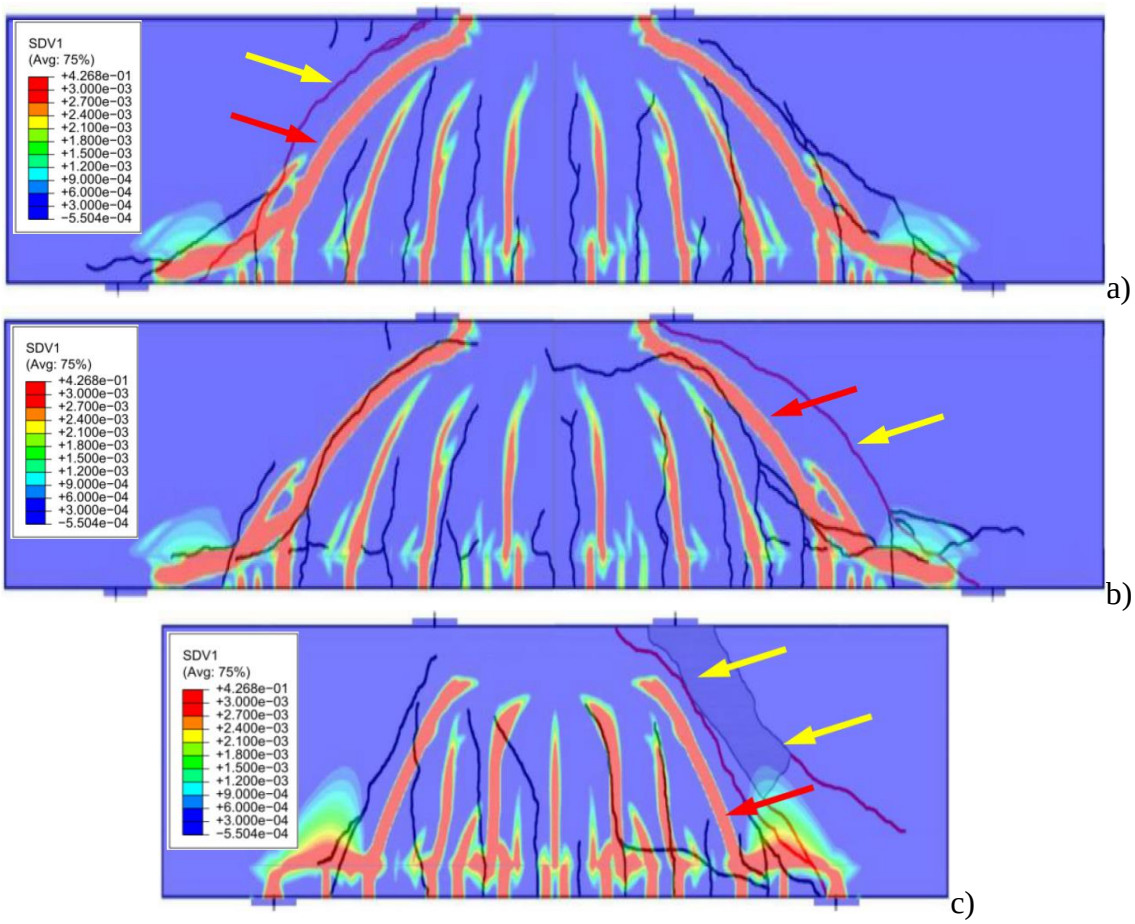

Fig.13: Contours of non-local equivalent strain measure $\bar{\varepsilon}$ with attached scale as compared with experimental cracks pattern for beams (D=360 mm): a) S2D36a72_1 and b) S2D36a72_2 (L_{eff}=1980 mm, a=720 mm, η_l=5.5, η_a=2) and c) S2D36a36 (L_{eff}=1260 mm, a=360 mm, η_l=3.75, η_a=1) (experimental critical diagonal crack is marked by red arrow, numerical critical diagonal localization zone is marked by yellow arrow, note that beams are not proportionally scaled and steel bars are not shown)

FIGURE 13

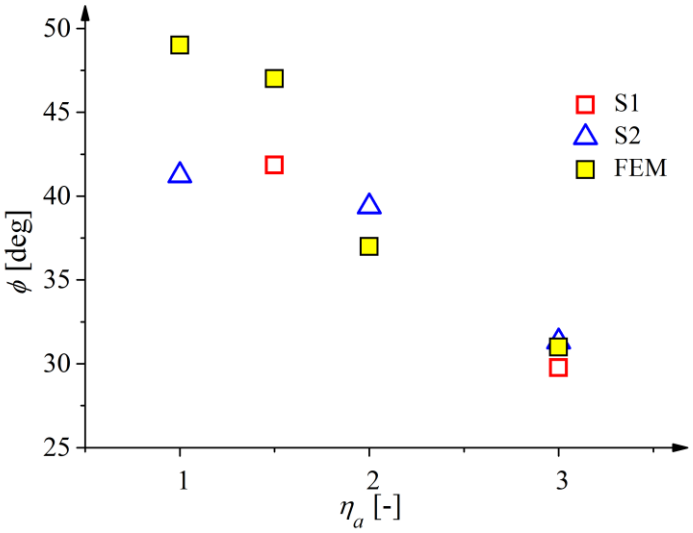

Fig.14: Diagonal failure crack/localized zone inclination ϕ to horizontal in RC beams for experimental series '1' (S1, square markers) and '2' (S2, triangle markers) versus ratio η_a as compared with FEM

FIGURE 14

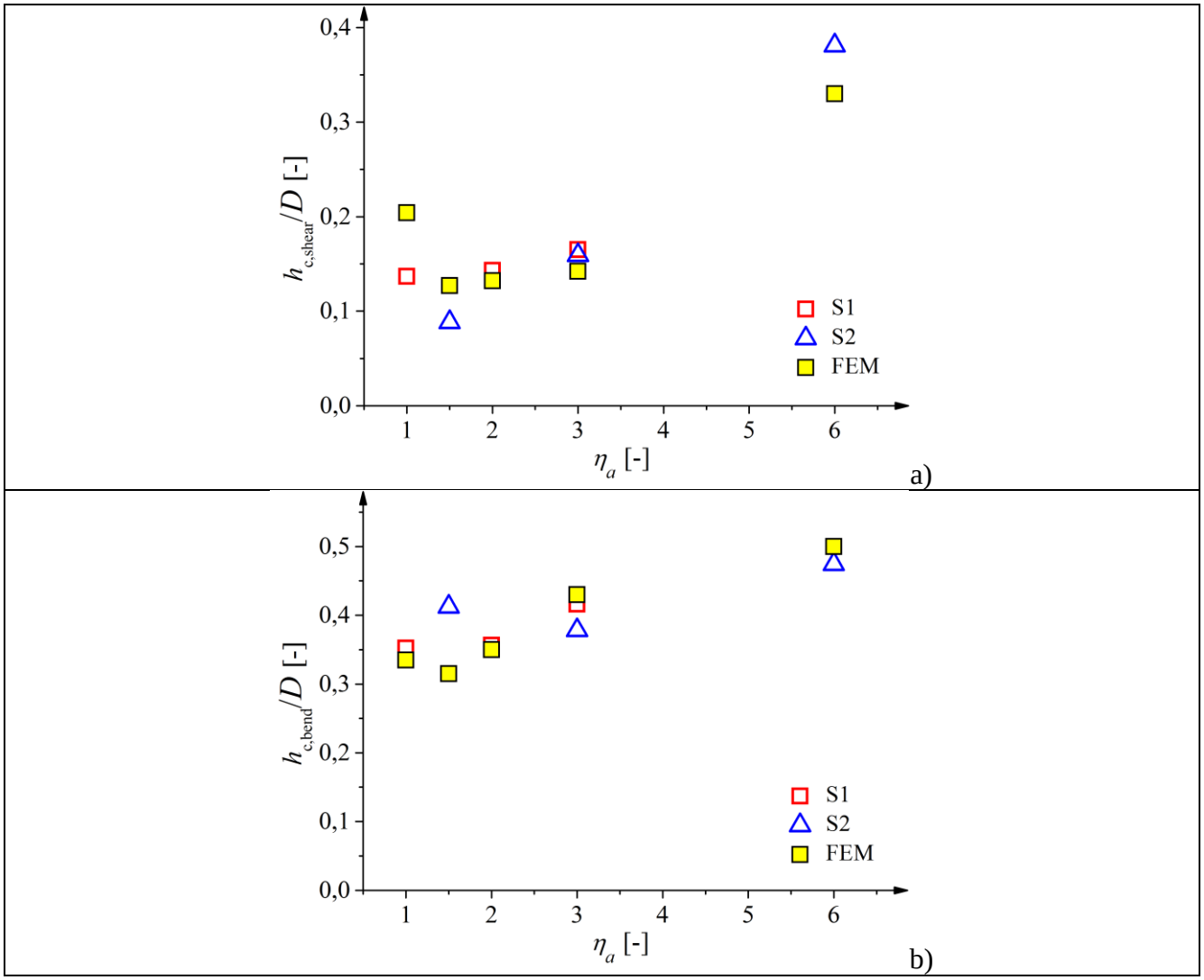

Fig.15: Experimental and calculated normalized height of compressive zone above shear and bending crack/localized zone for varying shear span parameter $\eta_a=a/D$ (S1 - experimental series '1', S2 - experimental series '2', note that beams for $\eta_a=6$ failed in flexural mechanism)

FIGURE 15

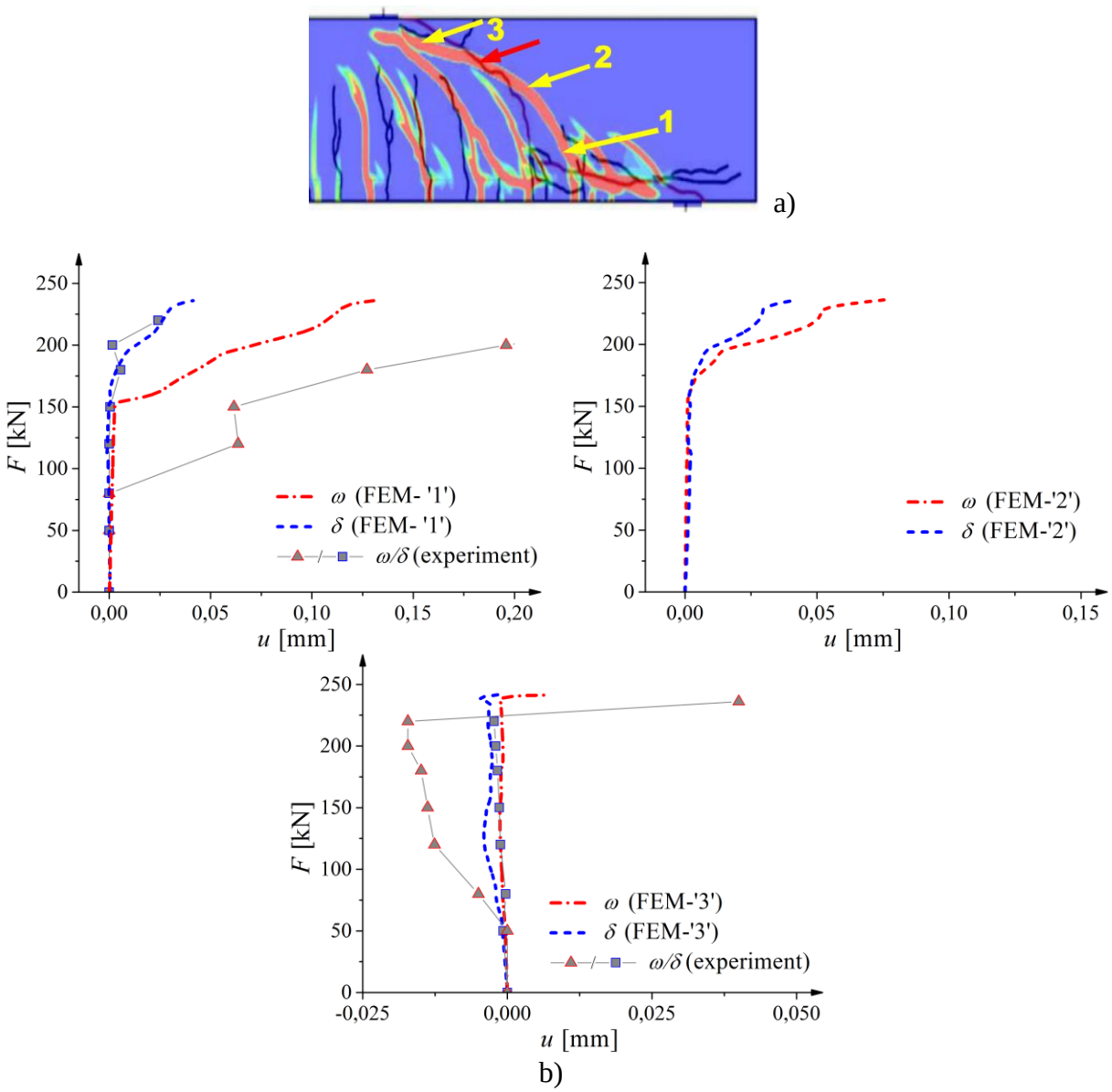

Fig.16: Calculated evolution of normal and tangential displacements at critical diagonal localization zone from FEM for beam S1D36a108 (η_a=3) as compared to experiments: a) locations (marked by yellow arrows) and b) vertical force versus displacements: ω - normal displacement, δ - tangential displacement (experimental critical diagonal crack is marked by red arrow)

FIGURE 16

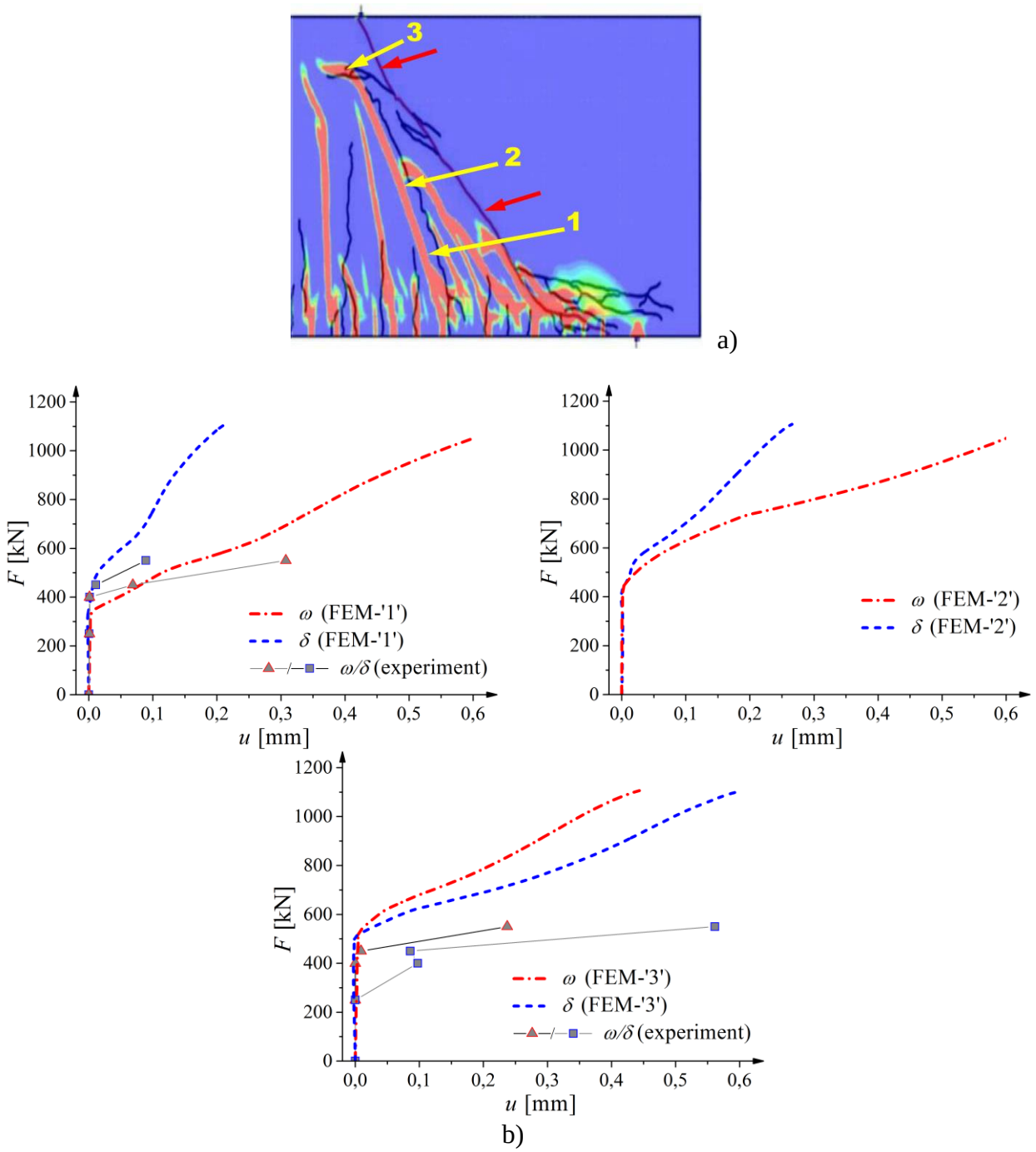

Fig.17: Calculated evolution of normal and tangential displacements at critical diagonal localization zone from FEM for beam S1D72a108 (η_a=1.5) as compared to experiments: a) locations (marked by yellow arrows) and b) vertical force versus displacements: ω - normal displacement, δ - tangential displacement (experimental critical diagonal crack is marked by red arrow)

FIGURE 17

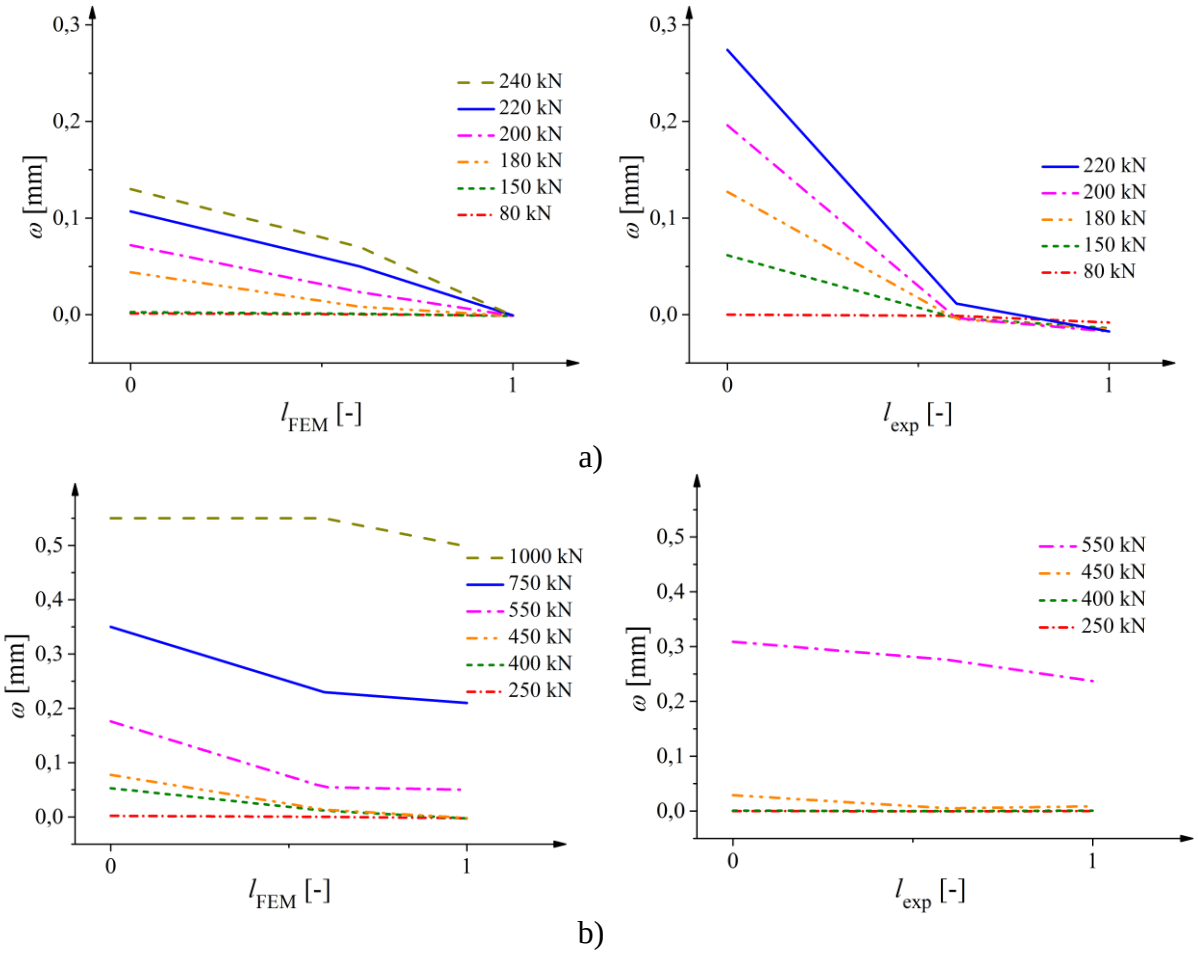

Fig.18: Comparison between calculated (left side) and experimental (right side) normal displacements ω along normalized critical diagonal crack/localization zone length l_{exp}/l_{FEM} for: a) beam S1D36a108 and b) beam S1D72a108 (horizontal coordinate 0 - point above reinforcement (point '1' in Figs.16 and 17) and horizontal coordinate 1 - point in upper beam region (point '3' in Figs.16 and 17)).

FIGURE 18

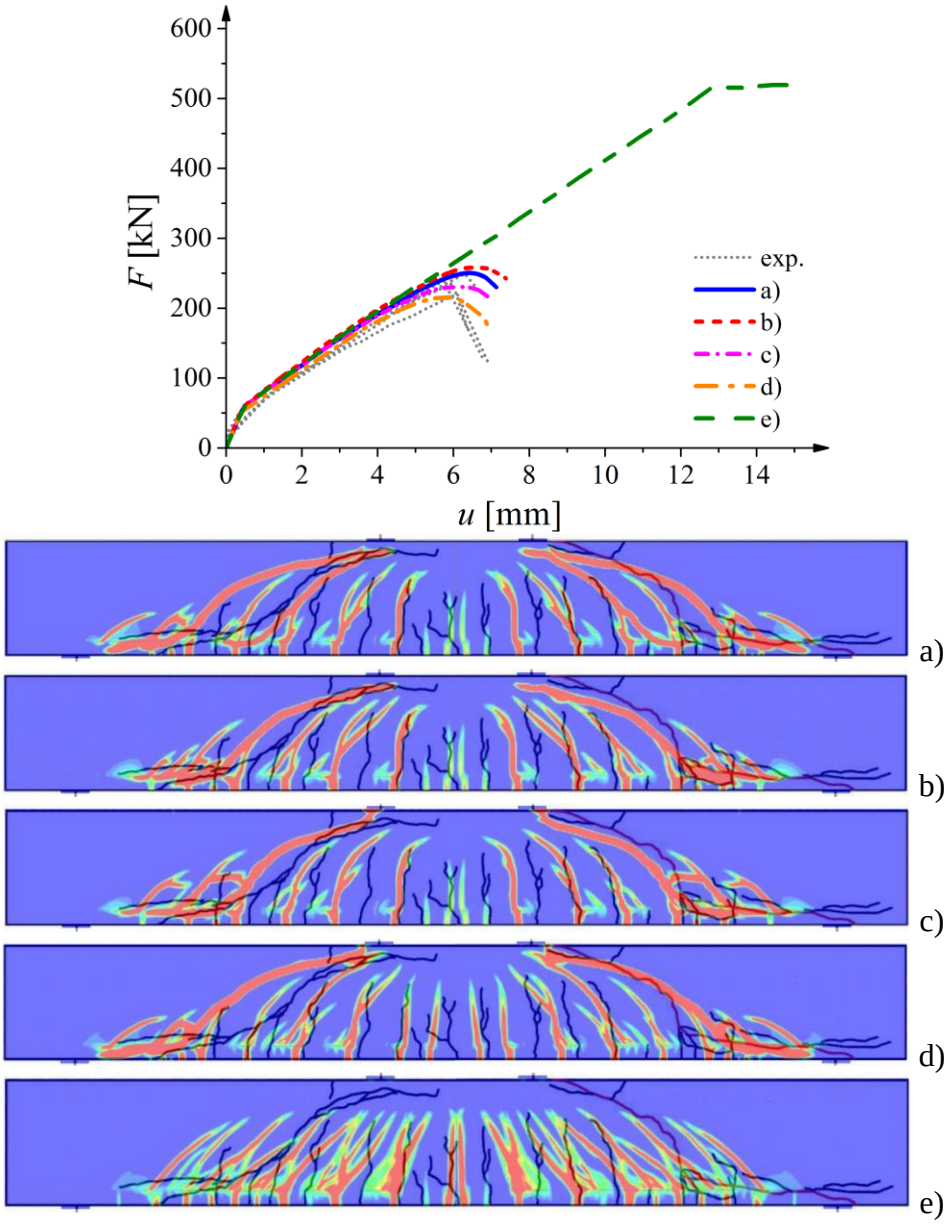

Fig.19: Calculated force-deflection curves and distributions of non-local equivalent strain measure from FE analyses using coupled elasto-plastic-damage with non-local softening as compared to experiments (beam S1D36a108, η_a=3): a) with basis set of material constants in Section 4, b) with softening constant β=60 (instead of β=85), c) with softening constants η_2=0.20 and δ_c=250 (instead of η_2=0.15 and δ_c=150) d) with $\kappa_0=7\times10^{-5}$ (instead of $\kappa_0=9\times10^{-5}$) and e) without plasticity and damage under compression

FIGURE 19

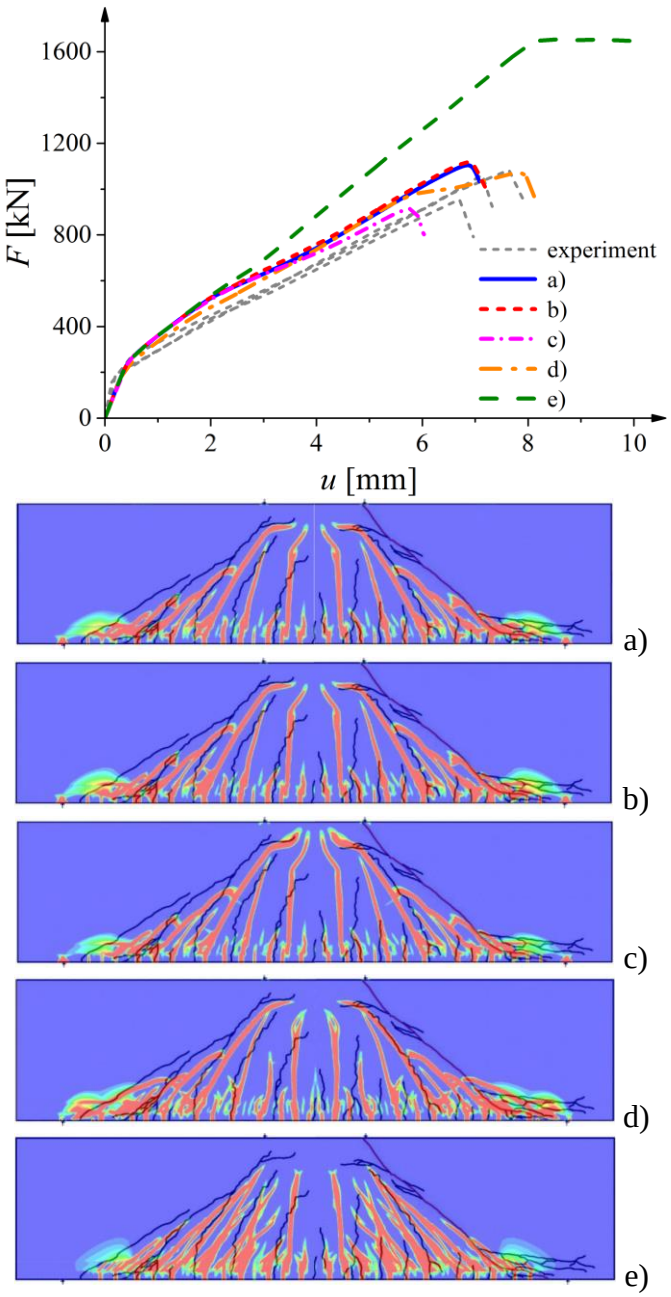

Fig.20: Calculated force-deflection curves and distributions of non-local equivalent strain measure from FE analyses using coupled elasto-plastic-damage with non-local softening as compared to experiments (beam S1D72a108, η_a=1.5): a) with basis set of material constants in Section 4, b) with softening constant β=60 (instead of β=85), c) with softening constants η_2=0.20 and δ_c=250 (instead of η_2=0.15 and δ_c=150), d) with $\kappa_0=7\times10^{-5}$ (instead of $\kappa_0=9\times10^{-5}$) and e) without plasticity and damage under compression

FIGURE 20

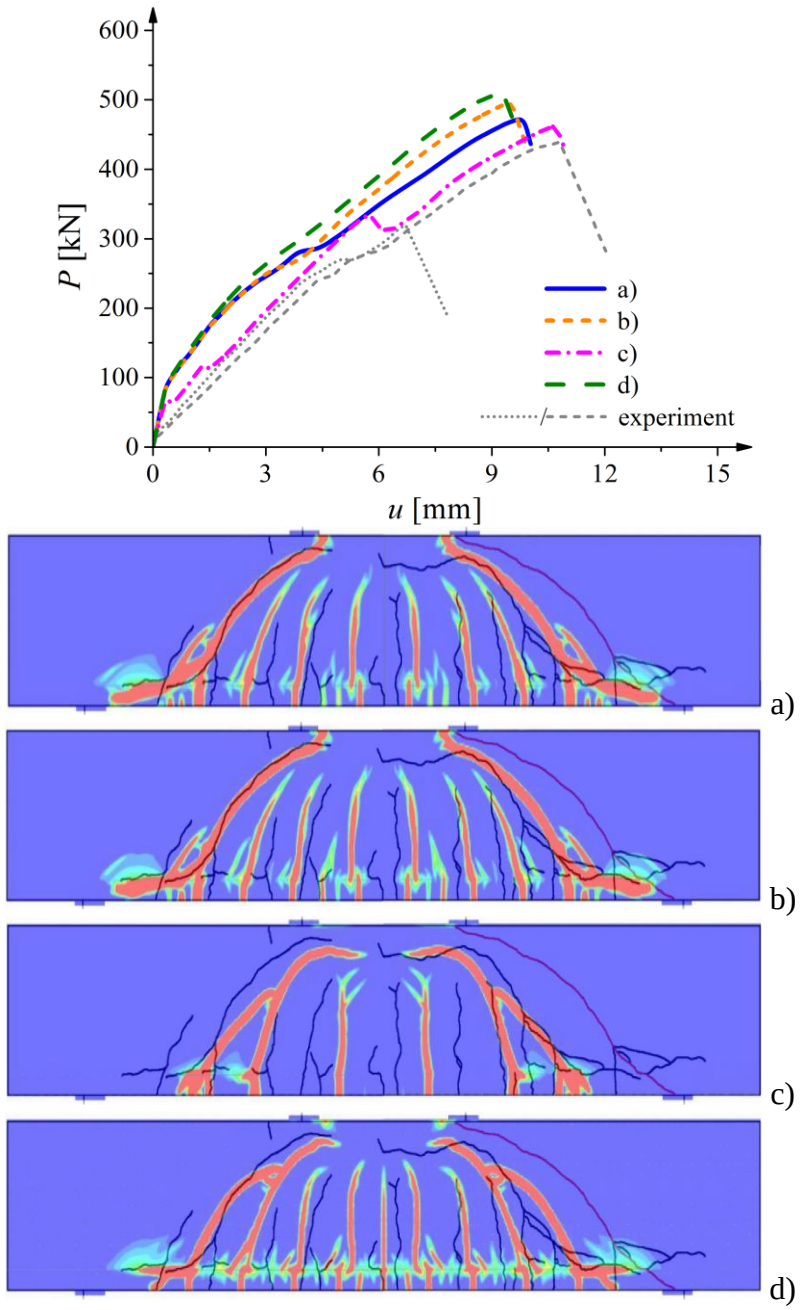

Fig.21: Calculated force-deflection curves (dotted line – experiments) and distributions of non-local equivalent strain measure from FE analyses using coupled elasto-plastic-damage with non-local softening as compared to experiments (beam S2D36a72, η_a=2) for bond-slip model of Fig.8: a) Eq.17 with δ_1=1 mm, δ_2=2 mm, and δ_3=5 mm (basic data), b) Eq.17 with δ_1=0.5 mm, δ_2=1.5 mm and δ_3=4.5 mm, c) Eq.17 with δ_1=100 mm, δ_2=200 mm and δ_3=500 mm and d) perfect bond model

FIGURE 21

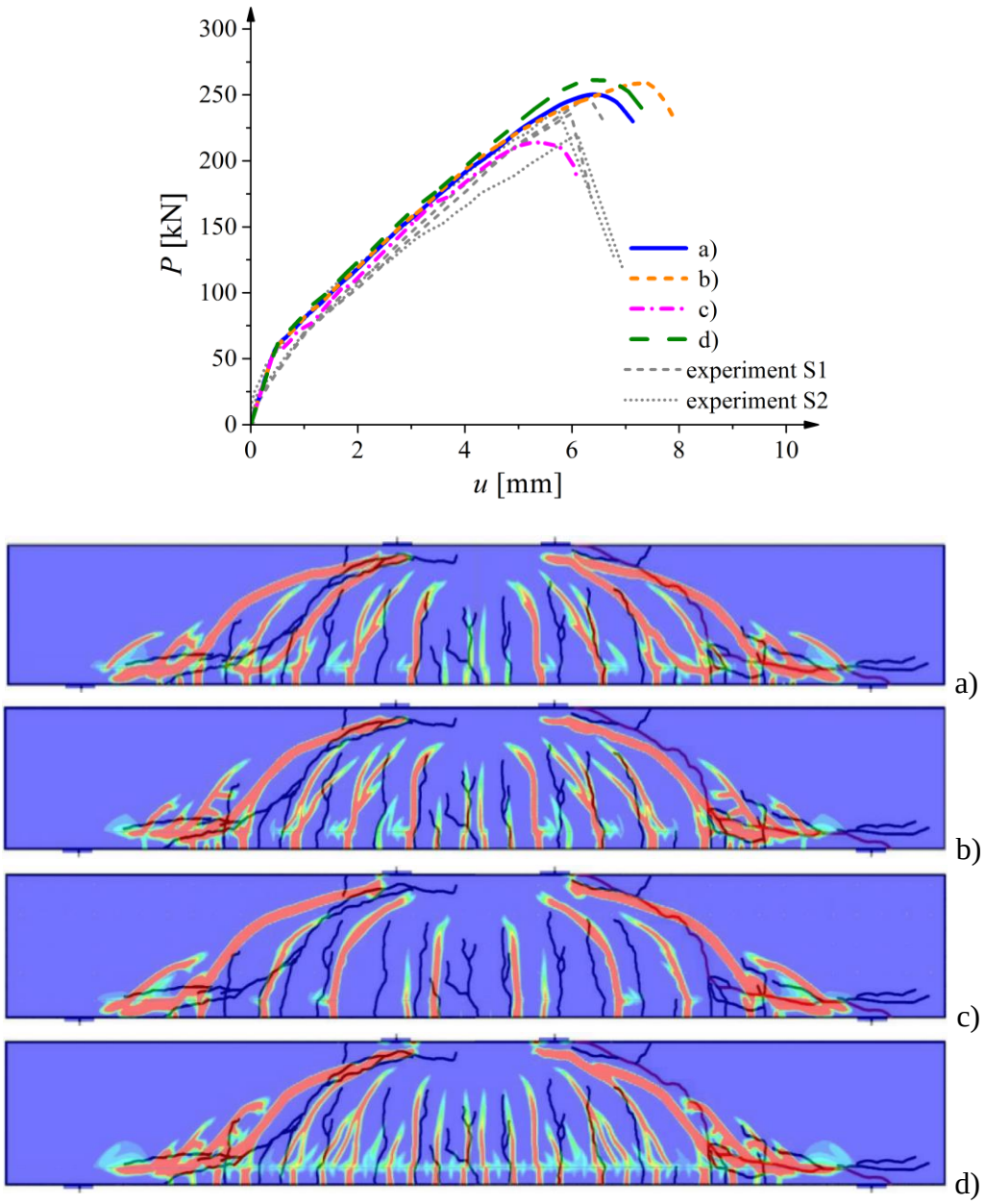

Fig.22: Calculated force-deflection curves (dotted line – experiments) and distributions of non-local equivalent strain measure from FE analyses using coupled elasto-plastic-damage with non-local softening as compared to experiments (beam S1D36a108, η_a=3) for bond-slip model of Fig.8: a) Eq.17 with δ_1=1 mm, δ_2=2 mm, and δ_3=5 mm (basic data), b) Eq.17 with δ_1=0.5 mm, δ_2=1.5 mm and δ_3=4.5 mm, c) Eq.17 with δ_1=100 mm, δ_2=200 mm and δ_3=500 mm and d) perfect bond model

FIGURE 22